The desmosomal cadherin Desmogon is necessary for the structural integrity of the Medaka notochord

Ali Seleit[1,2, #], Karen Gross[1,2], Michaela Woelk[1,], Camilla Autorino[1], Jasmin Onistschenko[1], Lazaro Centanin[1,#].

1 Animal Physiology and Development, Centre for Organismal Studies (COS) Heidelberg, Im Neuenheimer Feld 230, Heidelberg 69120, Germany.

2 The Hartmut Hoffmann-Berling International Graduate School of Molecular and Cellular Biology (HBIGS), University of Heidelberg, Heidelberg, Germany.

authors for correspondence: AS, ali.seleit@cos.uni-heidelberg.de and LC, lazaro.centanin@cos.uni-heidelberg.de

Running Title: *desmogon* is necessary for notochord integrity

Abstract

The notochord is an embryonic tissue that acts as a precursor to the spine. It is composed of outer sheath cells and inner vacuolated cells. Together they ensure the ability of the notochord to act as a hydrostatic skeleton until ossification begins. To date, there is still a paucity in our understanding of how the notochord cell types are specified and the molecular players controlling both their formation and maintenance remain poorly understood. Here we report that *desmogon,* a desmosomal cadherin, is essential for proper vacuolated cell shape and therefore correct notochord morphology. We trace *desmogon*+ precursors and uncover an early developmental heterogeneity that dictates the balance of vacuolated and sheath cell formation. We demonstrate that the growth of vacuolated cells occurs asynchronously and reveal the presence of distinct injury sensing mechanisms in the notochord. Additionally, using a small-scale F0 CRISPR screen we implicate uncharacterized genes in notochordal integrity.

Introduction

The notochord is the defining characteristic that unites all chordates (Lim et al. 2017; Satoh et al. 2012; Stemple 2005; Stemple et al. 1996; Corallo et al. 2018). Developmentally, it derives from the dorsal organizer region in vertebrate embryos (Stemple 2005; Ellis et al. 2013; Corallo et al. 2018). Subsequently, its constituent cells adopt a mesodermal fate and undergo convergent-extension movements (Satoh et al. 2012; Tada & Heisenberg 2012; Corallo et al. 2018; Stemple 2005; Stemple 2004). This results in a tube-like structure that runs along the anterior-posterior axis while simultaneously delimiting the dorso-ventral axis (Stemple 2005). In addition to providing structural support to embryos by acting as the major skeletal element during embryonic development (Stemple et al. 1996; Stemple 2005), it also has important signaling roles (Yamada et al. 1991; Yamada et al. 1993; Pourquie et al. 1993; Hebrok et al. 1998; Fouquet et al. 1997; Corallo et al. 2018; Stemple et al. 1996; Stemple 2005; Satoh et al. 2012). Indeed, patterning of adjacent tissues by the notochord is essential for correct morphogenesis to occur (Yamada et al. 1991; Yamada et al. 1993; Pourquie et al. 1993; Hebrok et al. 1998; Fouquet et al. 1997; Talbot et al. 1995; Stemple et al. 1996; Fleming 2004; Corallo et al. 2018). In vertebrates the notochord is a transient structure and a precursor to spine formation, it is eventually almost entirely replaced by vertebrae (Fleming 2004; Stemple 2005; Corallo et al. 2018; Lopez-Baez et al. 2018; Gray et al. 2014). Recently, it has been shown that correct spine patterning relies on segmentation cues present in the embryonic notochord (Wopat et al. 2018; Lleras Forero et al. 2018). This and other observations has led to the understanding that correct notochord morphogenesis is essential for normal spine formation (Fleming 2004; Lim et al. 2017; Wopat et al. 2018; Lleras Forero et al. 2018; Gray et al. 2014).

The notochord of all vertebrates studied to date (Ellis et al. 2014; Corallo et al. 2018) is formed of two cell-types: an outer sheath epidermal-like cell population and an inner vacuolated cell core (Stemple 2005; Corallo et al. 2018). The outer sheath cells cover the notochord tube and secrete ECM components that help in building and maintaining the peri-notochordal membrane

56 (Ellis et al. 2013; Corallo et al. 2018; Yamamoto et al. 2010; Lim et al. 2017), while the inner-
57 cells have large lysosomally-derived vacuoles that can withstand high hydrostatic pressure
58 (Ellis et al. 2013; Ellis et al. 2014). This ability to act as a hydrostatic skeleton is particularly
59 important in teleost fish as the strength and flexibility of the notochord is essential for proper
60 locomotion – which in turn is necessary for survival – as embryogenesis concludes (Stemple
61 et al. 1996; Ellis et al. 2014; Jiang & Smith 2007). A number of mutants affecting overall
62 notochord formation and differentiation have previously been described in ENU screens
63 (Stemple et al. 1996; Talbot et al. 1995). More recently, new players have been uncovered
64 that are important for vacuolated cell formation and maintenance (Lim et al. 2017; Garcia et
65 al. 2017). However, many decades after the first description of the notochordal cell types, there
66 is still a paucity in our understanding of the molecular players that control the correct formation
67 and maintenance of vacuolated and sheath cells and by extension the structural integrity of
68 the notochord (Ellis et al. 2013).
69
70 Here we uncover new regulators of correct notochord morphogenesis in vertebrates.
71 Desmogleins are a conserved family of calcium-binding cadherin transmembrane proteins.
72 They localize to cellular membranes and are important for establishing strong cell-cell contacts
73 and maintaining tissue integrity (Garrod & Chidgey 2008a). Structurally, they are part of the
74 intercellular desmosome junctions (Garrod & Chidgey 2008a) and are expressed in tissues
75 that undergo significant mechanical strain (Delva et al. 2009). We characterize the role of a
76 fish-specific Desmoglein, hereafter referred to as *desmogon*, that is expressed in the
77 notochord of Medaka and is to our knowledge the first Desmoglein reported to be present and
78 functional in chordate notochords. Indeed, the loss of *desmogon* causes vacuolated cell
79 defects and leads to structural deformities in the notochord. We generated a
80 Tg(*desmogon*:EGFP) to address the origin and growth dynamics of vacuolated cells by 4D-
81 imaging, a process revealed to be incremental and locally uncoordinated; vacuolated cells
82 behave like autonomous units. Interestingly, *desmogon* also labels early disc-shaped
83 notochord precursors that constitute a bipotent population. When analysed in 4D at the single-

84 cell level, however, we reveal that each progenitor is unipotent and generates either one
85 vacuolated cell or a number of sheath cells. In addition, exploiting the stable labelling of
86 vacuolated cells in our Tg(*desmogon*:EGFP), we uncover two distinct types of regeneration
87 responses in Medaka notochords, one spatially localized and the other global, that depend on
88 the type of injury sustained. Finally, we use Tg(*desmogon*:EGFP) to carry out a small scale
89 reverse-genetics screen on highly conserved and uncharacterized genes enriched in the
90 notochord (Briggs et al. 2018; Farrell et al. 2018). Using this fast and straight-forward
91 methodology we were able to implicate new players in correct notochord morphology in a
92 vertebrate model. This work and approach, we believe, could lead to a deepening of our
93 understanding of the origin of spine and vertebral defects.

Results

***desmogon* is a fish-specific desmosomal cadherin expressed in the notochord**

While searching for a stable marker for neuromast border cells (Seleit et al. 2017) we serendipitously came across a novel uncharacterized *desmog-2-like* gene (ENSORLG00000017110), which we named *desmogon*. The 5.3Kb long transcript of *desmogon* is distributed over 14 exons and encodes a protein with at least 3 desmosomal cadherin domains and one cytoplasmic cadherin domain (Supplementary Figure 1). Based on the amino acid sequence the expected sub-cellular localization is plasma membrane and it is predicted to function as a component of the inter-cellular desmosome junctions. A list of all known orthologues of *desmogon* suggests that this gene is fish-specific, as it is absent in all other sequenced chordates (materials and methods for details) (Supplementary Table 1 and 2). Among fish, the *desmogon* locus is conserved in the vast majority of teleost branches although interestingly, it seems to have been lost in Zebrafish and Tetraodon (as evidenced by the syntenic conservation of the surrounding genomic region) (Supplementary Figure 1). *In situ* hybridization showed *desmogon* to be highly expressed in the developing notochord of Medaka (Figure 1A). To gain a better understanding of the dynamic spatial expression of *desmogon* we generated the Tg(*desmog*:EGFP) (Figure 1B-F) by using a 2.2kb proximal promoter region that contained strong peaks of H3K4 methylation (Supplementary Figure 1). Confocal analysis of mosaic, injected *desmogon*:EGFP and of Tg(*desmogon*:EGFP) medaka embryos revealed EGFP expression in the developing notochord throughout embryogenesis (Figure 1B-F, Supplementary Movies 1 & 2), this expression persists in adult fish in a segmented pattern along the spine (data not shown). Within the notochord, *desmogon* labels vacuolated cells *(*Figure 1 C, F, arrows in Figure 1E, 1F) and a proportion of covering sheath cells *(*yellow asterisks in Figure 1E, 1F). The expression of a Desmoglein family member in vacuolated and sheath cells suggests the presence of desmosomes in both cell-types, therefore we followed an electron microscopy (EM) approach to characterise the notochord of 10 dpf *wild-type* medaka larvae at sub-cellular resolution. Previous studies reported the existence of caveolae in the cellular membrane of vacuolated cells in the zebrafish notochord

123 (Nixon et al., 2007; Lim et. al, 2017), which we confirmed is also present in medaka (Figure
124 1G, G'). Additionally, we observed the presence of desmosomes mediating the physical
125 association of neighboring vacuolated cells (Figure 1G, G'), presumably to enhance their inter-
126 cellular adhesion capacities. Desmosomes were also found connecting sheath to vacuolated
127 cells (Figure 1H, I), and sheath to sheath cells (Figure 1I). Altogether, our results reveal the
128 expression of an uncharacterised Desmoglein-like family member in the two cell types of the
129 notochord that concurrently display desmosomes on their cellular membranes.
130

131 **Extension of medaka notochord occurs via asynchronous vacuolated cell growth**
132
133 The Tg(*desmog*:EGFP) allowed us to follow the axial extension of the notochord as the embryo
134 develops. Notochord extension is mediated by the growth of vacuolated cells (Ellis et al., 2013;
135 Corallo et al., 2018) that not only increase in size but also change their circular morphology
136 into a more oblique shape as the notochord matures (Figure 2A, B) (N>10 notochords). During
137 notochordal extension we observed that vacuole size in adjacent cells is not homogenous
138 (Figure 2A), suggesting that the growth of vacuolated cells could be asynchronous. Indeed, by
139 classifying vacuoles according to their size we were able to detect an intermingled distribution
140 of vacuole area along the central, growing part of the notochord (Supplementary Figure 2A).
141 We tracked vacuolated cell growth over time using transmitted, confocal and single plane
142 illumination microscopy (SPIM) (Krzic et al., 2012) and observed that neighboring vacuolated
143 cells grow anisotropically and asynchronously over time (Figure 2C, Supplementary Figure 2B
144 for quantification) (Supplementary Movies 3, 4 and 5) in a process that appears to be
145 irreversible (N>50 cells in 10 embryos). Interestingly, we also report that the global extension
146 of the medaka notochord occurs in both the anterior and posterior directions. The growth of
147 vacuolated cells in the central part of the notochord displaces anterior and posterior neighbors
148 to their respective ends of the tube (Figure 2D-F', Supplementary Movies 6-10). Overall, we
149 show that the medaka notochord extends in a bidirectional manner, which is driven by a local
150 asynchronous growth of vacuolated cells from the central section of the tube.
151

152 **Unipotency of *Desmogon*+ disc shaped precursors**

153 The extension of the notochord is complemented by the addition of new differentiated cells at
154 the posterior tip, originating from so-called disc-shaped precursors (Dale and Topczewski
155 2011; Yamamoto et al., 2010; Melby et al.,1996). The population of disc-shaped-precursors
156 was previously shown to generate both differentiated cell types (Yamamoto et al., 2010; Melby
157 et al., 1996), and therefore constitutes a bi-potent population. While analysing sparsely labelled
158 notochords of medaka larvae that were injected with *desmogon*:EGFP (Figure 3A, B) at the
159 two cell stage, we noticed that clusters tended to contain either vacuolated or sheath cells
160 (N=41 sheath cells clusters, N=39 vacuolated cell clusters, N=80/93 cell-type specific cluster
161 and N=13/93 clusters containing both cell types, N=93 clusters in 26 mosaic larvae). These
162 results suggest that under physiological conditions disc-shaped precursors might be bi-potent
163 as a population, but fate-restricted as individual cells. To test this hypothesis directly, we
164 followed the process by 4D imaging. Disc precursors are labelled in the Tg(*desmogon*:EGFP)
165 (Figure 1B, Figure 3 A and C, Supplementary Movie 10 and 11), which allowed us to follow
166 the notochordal differentiation process dynamically at the single cell level. We observed two
167 distinct, mutually exclusive cellular behaviours in *desmogon*+ disc-shaped precursors. On the
168 one hand, they can directly generate a single vacuolated cell (Figure 3C-C'', magenta dot)
169 (Supplementary Movie 10-12) (N=17/23 cells in 3 embryos). These cells did not divide
170 throughout our imaging and therefore constitute a post-mitotic cell type (N=3 embryos at 4 dpf,
171 and N=2 embryos at 3dpf image for 24h, N>50 cells) (Supplementary movie 3), as was
172 reported for zebrafish vacuolated cells (Garcia et al., 2017). On the other hand, disc-shaped
173 precursors can also undergo a dorso-ventral symmetric division leading to the exclusive
174 formation of sheath cells (Figure 3C-C'' yellow dots) (Supplementary Movie 12) (N=6/23 cells
175 in 3 embryos), indicating that disc-shaped precursors are unipotent in medaka.

176

177 To test whether the observed unipotency of disc-shaped precursors is a medaka-specific
178 feature we decided to explore the same process in zebrafish. Even though a *desmogon*
179 orthologue does seem to be present in *Danio rerio*, we observed EGFP-labelled disc-shaped

180 precursors, vacuolated and sheath cells in *desmogon*:EGFP zebrafish injected embryos
181 (Supplementary Figure 3, and Supplementary Movie 13). This indicates that the transcriptional
182 machinery driving expression of medaka *desmogon* is conserved in distantly related teleost
183 fish. Live-imaging of embryos with EGFP+ clones in the undifferentiated notochord revealed
184 that similar dynamics govern the differentiation process in zebrafish as in Medaka. Disc-
185 shaped *desmogon*+ precursors directly differentiate into vacuolated cells (N=8 cells in 6
186 embryos) that will not undergo mitosis throughout our imaging (N>10 cells in 6 embryos).
187 Additionally, a closer look at the notochordal differentiation dynamics in zebrafish revealed that
188 the birth and growth of vacuolated cells is governed by the same dynamics as we report in
189 Medaka (from disc-shaped precursors that differentiate and grow incrementally in a locally
190 unsynchronized manner) (N>10 cells n=6 embryos) (Supplementary movie 13-15).
191 Additionally, and as we report for medaka, disc-shaped precursors in zebrafish form sheath
192 cells exclusively after undergoing a dorso-ventral symmetric division (N=16 cells in 6 embryos)
193 (Supplementary Figure 3, Supplementary movie 14 and 15). In contrast to the post-mitotic
194 nature of vacuolated cells, sheath cells continue to divide long after acquiring their
195 characteristic morphology and peripheral position. Interestingly in both medaka and zebrafish
196 we also observed the presence of newly formed sheath cells that do contain small vacuoles
197 (n>10 cells in n=6 embryos in Zebrafish and n=3 embryos in Medaka) (Supplementary Movie
198 14 and 16), suggesting that this feature could reflect morphologically distinct sub-populations
199 of sheath cells. Overall, our results show on the one hand that *desmogon*:EGFP is a suitable
200 tool to study early aspects of notochord differentiation in distantly related teleosts, and
201 demonstrates the presence of unipotent, fate-restricted disc-shaped precursors that
202 exclusively generate either vacuolated or sheath cells. Since both vacuolated and sheath cells
203 come from unipotent precursors and since we and others have shown that these disc-shaped
204 precursors are exhausted by the end of notochordal development (Ellis et al. 2013; Corallo et
205 al., 2018), we wondered whether and how vacuolated cells can be replaced after injury of
206 mature Medaka notochords.
207

208 **Local regenerative response after targeted vacuolated cell loss in medaka**

209 Recent findings using a number of injury paradigms have reported that zebrafish can efficiently
210 regenerate the notochord (Garcia et al. 2017; Lopez-Baez et al., 2018). Given the differences
211 in regenerative capacities among teleosts (Lust & Wittbrodt 2018; Ito et al. 2014; Lai et al.
212 2017), we used Tg(*desmogon*:EGFP) to address the response to local notochord injuries in
213 medaka. Spatially targeted and precise multi-photon laser ablation of 6-10 vacuolated cells of
214 5-6 dpf Tg*(desmogon:*EGFP*)* embryos resulted in the specific loss of cells in the area of injury
215 (Figure 4A-A'', Supplementary Figure 4 Supplementary movie 17 and 18). Both sheath and
216 vacuolated cells outside the ablated zone retain a normal morphology and the overall integrity
217 of the notochord is unaffected (Figure 4A-B, entire Z-stacks in Supplementary Movie 19 and
218 20). Two days post injury we observed the appearance of small *desmogon*+ vacuolated cells
219 specifically in the area of injury (Supplementary Figure 4, Supplementary movie 19) (n=8
220 embryos). Interestingly, the overall morphology, presence of a small vacuole, and EGFP+
221 expression of these cells was highly reminiscent of the earliest vacuolated sheath cells we
222 observed during development in both medaka and zebrafish notochords, suggesting that the
223 regenerative response is mediated by the same cell type in both species (Garcia et al. 2017).
224 The small vacuolated cells grow in size over time as assessed at 5 days post injury (Figure
225 4C, Supplementary movie 20) (N=8 embryos), this growth followed the same asynchronous
226 rationale we observed under physiological conditions in Medaka. Overall, our results indicate
227 that Medaka notochords can mount a robust and local regeneration response to vacuolated
228 cell loss, which is spatially restricted to the initial injury site.

229

230 **Global regeneration responses following peri-notochordal membrane injury**
231
232 The perinotochordal membrane is a thick ECM layer that ensheathes the notochord and helps
233 to maintain its integrity (Ellis et al. 2013; Corallo et al. 2018; Yamamoto et al. 2010; Lim et al.
234 2017). To test the effect of a sudden loss of hydrostatic pressure within the notochordal tube,
235 we ablated the lower lining of the peri-notochordal membrane (Figure 4 C-C', Supplementary
236 Figure 4, Supplementary movie 21). Two days post-injury we observed *desmogon*+ cells

237 leaking outside of the notochord tube, indicating that the lower lining of the notochordal
238 membrane failed to be repaired (Supplementary Figure 4). Given the post-mitotic nature of
239 vacuolated cells and the dynamics of regeneration shown earlier, the local leakage at the initial
240 injury site decreases the number of vacuolated cells that remain in the tube. This was
241 accompanied by the appearance of small desmogon+ cells containing a vacuole as reported
242 for the local response, although here these are found anterior and posterior to the initial
243 targeted injury site (Figure 4 C-C'', Supplementary Figure 4). Five days post-injury the leakage
244 of notochord vacuolated cells continued, forming a herniated structure, and resulting in a
245 significant perturbation of notochord morphology. Small vacuolated cells persisted anterior and
246 posterior to the injury site (Figure 4D-D'') (n=3). Overall, we conclude that injury to the peri-
247 notochordal membrane, which cannot be efficiently repaired in Medaka, leads to cell leakage
248 and a perturbed notochord morphology. This in turn triggers a global regeneration response
249 that is not spatially restricted to the initial injury site.
250
251 ***Targeted CRISPR screen uncovers novel regulators of notochord integrity***
252 In addition to structural damage sustained by the notochord due to targeted laser ablation, we
253 wondered whether similar phenotypes can be observed by genetic perturbations. It has
254 recently been reported that F0 CRISPR phenotypes concur with the ones observed in stable
255 mutant lines (Wu et al. 2018; Lischik et al. 2018; Trubiroha et al. 2018). We therefore decided
256 to use the Tg*(desmogon:*EGFP*)* as a fast and straight-forward read-out of notochordal defects.
257 Exploiting the recently generated single-cell transcriptome data from Zebrafish (Briggs et al.
258 2018; Farrell et al. 2018) we chose a number of well annotated and poorly characterized genes
259 that were strongly conserved across vertebrates and highly expressed during Zebrafish
260 notochord morphogenesis (*arrdc3a, kcnk6, pmp22b, si:dkey- 261h17.1 and vgll2b*) and
261 designed 2 gRNAs targeting selected exons for each gene (for details of selection criteria see
262 materials and methods). For *vgll2b* this resulted in 55% of injected embryos showing
263 morphological defects in notochord shape and integrity including twisting and bending of the
264 notochord tube (Figure 5B-B'', Table 1). Targeting *arrdc3a* resulted in 30% of injected embryos

265 showing disruption in notochordal integrity, with strong phenotypes including buckling and
266 kinking (Figure 5C-C'' and Table 1). Targeting *kcnk6, si:dkey- 261h17.1, pmp22b* with the
267 same approach resulted in strong phenotypes on the notochord during embryogenesis
268 (Supplementary Figure 6) but additionally all three showed significant pleiotropic effects
269 (Stemple et al. 1996), including general growth retardation, shorter body axes and gross
270 morphological defects (for quantifications on all injections and the phenotypes observed see
271 Table 1). In addition, we also targeted the teleost specific *desmogon* with 3 gRNAs to address
272 whether it has any functional role during notochord morphogenesis and/or maintenance
273 (Supplementary Figure 5). Phenotypes in *desmogon* crispants included the loss of notochord
274 integrity and shape as revealed by kinking and buckling along the notochord tube (Figure 5D-
275 E', Table 1). In conclusion, using a straight-forward reverse-genetics approach we have
276 uncovered novel and conserved regulators of notochord morphogenesis and maintenance in
277 vertebrates. The use of the Tg(desmogon:EGFP) line allowed us to complement our gross
278 description of the notochordal phenotypes with a more detailed view on the cellular
279 organization of the tissue (Figure 5 F). We noticed that unlike the other candidate genes
280 *desmogon* crispants specifically exhibited defects in vacuolated cell morphology (Figure 5 E').
281 We therefore decided to take a closer look at the cellular defects in *desmogon* mutant
282 notochords.
283
284
285 ***Desmogon* crispants and stable mutants exhibit notochordal lesions of collapsed**
286 **vacuolated cells**
287
288 CRISPR/Cas9 injection into Tg*(desmogon:*EGFP*)* resulted in lesions containing collapsed
289 vacuolated cells along the length of the notochord, which were absent in embryos injected with
290 control *oca2* gRNAs (Figure 6 A-C, Supplementary Movies 24, 25) (Lischik et al. 2018). The
291 vast majority of injected embryos survived until stage 42 and no obvious pleiotropic effects
292 were detected, suggesting a notochord-specific role for Desmogon. A proportion of F0 injected
293 embryos that survived to adulthood showed strong signs of bending and defective spine

294 formation (data not shown). We therefore decided to perform alizarin-red bone stainings on
295 *desmogon* crispants and mutants. This revealed the presence of defects in vertebrae (smaller,
296 misshaped, and fused vertebrae) (Figure 6 F-H), linking proper vacuolated cell shape
297 conferred by Desmogon to correct spine formation in Medaka. The described phenotypes for
298 the F0 injected *desmogon* crispants were consistently recapitulated in *desmogon* mutants
299 (Figure 6A-D, Supplementary Movies 22, 23 and Supplementary Figure 5 for alleles isolated
300 in the stable mutant line). A closer analysis of the phenotypes affecting embryos with collapsed
301 notochords revealed the presence of larger lesions that were consistently filled with
302 *desmogon*+ small vacuolated cells (Supplementary Movie 22 & 23). To gain a better
303 understanding of the structural phenotypes observed in *desmogon* mutants, we decided to
304 perform electron microscopy (EM) on mutant notochords. We first focused on the presence
305 and structural integrity of mutant desmosomes, and could not observe any obvious phenotype
306 when compared to *wild-type* desmosomes (Figure 7 A-C). Longitudinal sections on wild-type
307 notochords were characterised by the typical highly ordered array of vacuolated cells (Figure
308 7D). This contrasts with the structural disorganization present in lesioned areas of the
309 *desmogon* mutant notochords (Figure 7 E-E'). EM data also showed the presence of
310 vacuolated cells of appreciably different sizes (Figure 7 E-E', arrows), evidence of vacuolated
311 cell collapse (Figure 7F-F'), and invasion of sheath cells into the central notochord tube that
312 indicates the possible triggering of a regenerative response in the lesioned area (Figure 7 E-
313 G asterisk). In addition to being a marker for vacuolated cells, we therefore believe that
314 *desmogon* has a functional role in proper notochord integrity and shape. Its loss leads to
315 vacuolated cell collapse and the appearance of lesions that contain small vacuolated cells, this
316 can in turn lead to gross morphological defects in the notochord.
317
318 Interestingly, the position, number and size of lesioned areas in the notochord (both in the
319 injected and stable mutant line) were variable among siblings. We therefore wondered whether
320 the appearance and position of the vacuolated cell defects in *desmogon* mutants depended
321 on the mechanical stress the notochord endures during tail movement and bending, as has

322 been recently reported for caveolae mutants in Zebrafish (Lim et al., 2017). This could be
323 particularly relevant in Medaka due to the long embryogenesis, larger overall size and more
324 tightly confined space within a stronger chorion as compared to zebrafish. Importantly, Medaka
325 embryos regularly bend their tails during development (Iwamatsu 2004). To test whether
326 movement is required for the appearance and/or severity of the collapsed vacuolated cell
327 phenotype, we injected *alpha-bungarotoxin* mRNA into *desmogon* mutants (Lischik et al.
328 2018). This led to the transient loss of movement throughout embryogenesis that was later
329 restored at 9-10 dpf when the toxin levels dampened. Injected embryos and un-injected
330 controls were removed from the chorion 3dpf and followed day by day for the appearance of
331 notochordal lesions. In total, 21/21 alpha-bungarotoxin injected *desmogon* mutant did not show
332 any signs of movement and did not display any collapsed vacuolated cell phenotypes
333 throughout embryogenesis. This contrasted with the earlier appearance of notochordal lesions
334 in un-injected *desmogon* mutants (with tail movements) on day 6-8 post fertilization. Of the 21
335 alpha-bungarotoxin injected *desmogon* mutants, 16 showed lesions of collapsed vacuolated
336 cells in the notochord only upon regaining the tail movement, 2 fish died before any visible
337 movement and did not show any lesions and 3 fish did not show any visible lesions even after
338 movement. The results strongly suggest that the collapse of vacuolated cells occurs after the
339 specification and growth phases and that the phenotype largely depends on, and is
340 exacerbated by, the mechanical stress induced by tail bending and movement. This is in line
341 with previous reports in other mutants affecting vacuolated cell shape and integrity in zebrafish
342 (Lim et al., 2017). Overall, we report that Desmogon is a necessary desmoglein in maintaining
343 proper vacuolated cell morphology specifically during the intense mechanical stress imposed
344 by the physiological movement of Medaka fish.

Discussion

Desmogleins are a conserved family of desmosomal cadherins that localize to the plasma membrane of cells (Garrod & Chidgey 2008b; Delva et al. 2009). They are a constituent part of desmosomes and are important mediators of strong inter-cellular adhesion. Indeed, desmosomes have been shown to be expressed in cell types that operate under significant mechanical strain (Garrod & Chidgey 2008b; Delva et al. 2009). Loss of desmosomal function leads to disruption of tissue integrity (Garrod & Chidgey 2008a). The notochord is a tissue that is constantly assailed by strong mechanical stresses (Lim et al. 2017; Garcia et al. 2017; Corallo et al. 2018). It is able to withstand those pressures primarily because of its structural organization: large vacuolated cells on the inside of the tube are surrounded by a strong peri-notochordal membrane formed by sheath cells (Lim et al. 2017; Yamamoto et al. 2010; Koehl et al. 2000; Adams et al. 1990). Our study on *desmogon,* a fish-specific desmosomal cadherin, is the first showing a desmoglein family member expressed and functional in vertebrate notochords.

desmogon **is necessary for correct notochord morphology in Medaka**

The structural demands on teleost notochords are particularly high given that larvae need to swim and feed as soon as embryogenesis concludes (Jiang & Smith 2007; Stemple et al. 1996; Ellis et al. 2014). Significantly, this happens before the ossification and formation of spines (Corallo et al. 2018; Lleras Forero et al. 2018; Wopat et al. 2018; Fleming 2004; Gray et al. 2014). This could explain the specific allocation of this desmoglein family member expression to the notochord. To test whether *desmogon* has a functional role in the Medaka notochord we targeted it by CRISPR/Cas9 and observed flattened vacuolated cells and lesions along the length of the notochord. This could either be a sign of collapsed vacuolated cells (Lim et al., 2017) or a failure of vacuolated cells to properly form. Our EM data on lesioned mutant notochords and the *alpha-bungarotoxin* experiment strongly suggest that the phenotype results from the local collapse of vacuolated cells due to movement. Interestingly, in areas that

374 contained larger lesions (both in injected fish and in stable mutants), we consistently observed
375 the appearance of small vacuolated cells. This is highly reminiscent of results we report from
376 the regeneration experiments and suggests that the collapse of *desmogon* mutant vacuolated
377 cells can trigger a regenerative response. Indeed, EM results on lesioned notochords shows
378 evidence of invading sheath cells. Our results indicate that *desmogon* is necessary for the
379 maintenance, but not the formation or growth, of vacuolated cells. Paralyzed desmogon mutant
380 embryos showed no signs of notochordal disruption or vacuolated cell defects. In general, we
381 observed a strong correlation between the size of the mutant lesion and the structural integrity
382 of the notochord, bigger lesions invariably led to buckling and kinking of the notochord tube.
383 Our results are in line with previous observations that have shown that correct vacuolated cell
384 morphology is essential for the notochord to withstand the high mechanical stresses it faces
385 (Lim et al. 2017; Ellis et al. 2013; Garcia et al. 2017; Fleming 2004; Adams et al. 1990). Failure
386 of properly building up and maintaining the high hydrostatic pressure inside the notochord tube
387 leads to bending and buckling along the length of the notochord (Ellis et al. 2013; Corallo et
388 al. 2018). Intriguingly, the cellular phenotype we report for *desmogon* mutants in Medaka is
389 highly reminiscent of the caveolae mutant phenotype in zebrafish (Lim et al. 2017). This
390 suggests that the notochord as a system might have multiple independent buffering capacities
391 against vacuolated cell collapse under mechanical stress. Given the essential role of the
392 notochord in the early survival of teleost larvae it is possible that these buffering capacities
393 evolved to imbue the notochord with more strength by acting synergistically and buffering
394 against the malfunctioning of one component. Lastly, we show that lesioned vacuolated cells
395 in *desmogon* mutant notochords lead to a disruption of proper vertebral segmentation
396 complementing recent findings in the field (Lim et al. 2017; Wopat et al. 2018; Lleras Forero et
397 al. 2018; Gray et al. 2014). Our results demonstrate that the presence of *desmogon* in the
398 Medaka notochord is necessary for correct vacuolated cell shape and by extension proper
399 notochord (and spine) morphology and integrity.
400
401 The fact that *desmogon* is present in the vast majority of teleost branches argues that it has a

402 conserved role in notochord maintenance in fish. However, there are two intriguing exceptions,
403 *desmogon* has no detectable orthologues in Tetraodon or in Zebrafish. It seems likely that both
404 fish have lost *desmogon* through the course of their evolution, this interpretation is supported
405 by the fact that we can identify syntenic genomic regions that do not contain *desmogon.* It
406 remains a formal possibility, however, that an orthologue with a highly divergent nucleotide
407 sequence exists in Zebrafish and Tetraodon. It would be interesting to see whether other
408 desmosomal cadherins have taken over the notochordal role of *desmogon* in those species.
409 Indeed, other desmosomal cadherin family members have been implicated in notochord
410 integrity in Zebrafish (Goonesinghe et al. 2012), although mutants display earlier gastrulation
411 defects that complicate the proper characterisation of notochordal phenotypes. Interestingly,
412 injecting our medaka *desmogon* partial promoter driving GFP in Zebrafish results in vacuolated
413 and sheath cell labelled clones. This suggests that the core transcriptional machinery driving
414 tissue-specific expression of *desmogon* remains in place and active in Zebrafish. It would be
415 of interest to investigate when the deployment of desmosomal cadherins in notochords arose
416 during evolution and how wide-spread its usage is among the different chordate clades.
417
418 ***Tg(desmogon:EGFP)*as a screening tool for genes involved in proper notochord**
419 **morphology**
420
421 It has been reported that most biomedical research today focuses heavily on a limited number
422 of genes, leaving behind potentially important genes understudied (Stoeger et al. 2018).
423 Making use of our newly generated transgenic line in combination with the recently published
424 and publicly available single cell transcriptomics data from vertebrate embryos (Briggs et al.
425 2018; Farrell et al. 2018), we attempted to address this imbalance. To do so we performed a
426 small scale F0 CRISPR screen, the efficacy of which has been recently demonstrated in
427 Zebrafish (Wu et al. 2018) and confirmed in other fish species (own observations and personal
428 communications). Indeed, recent work in Medaka (Lischik et al. 2018), in addition to our results
429 from *desmogon* mutants, argues for the use of F0 injected embryos as a method to analyse
430 tissue-specific phenotypes. Briefly, we focused on conserved well-annotated genes that were
431 highly and differentially expressed in developing notochords. We addressed whether they

432 might be involved in proper notochord morphology by using the *desmogon:GFP* line as a fast
433 and straight-forward read-out for notochord shape and integrity. Broadly, the targeted genes
434 fell into two categories. *kcnk6, si:dkey- 261h17.1, pmp22b* constituted the first category and
435 showed strong pleiotropic effects in addition to notochordal defects. Delineating the cause of
436 the pleiotropy is difficult given the essential signaling role of the notochord. (Yamada et al.
437 1991; Yamada et al. 1993; Pourquie et al. 1993; Hebrok et al. 1998; Fouquet et al. 1997;
438 Corallo et al. 2018; Stemple et al. 1996). The observed defects could either arise from the
439 inability of the notochord to correctly pattern adjacent tissue or from notochord independent
440 roles for these genes during embryogenesis. This makes assigning causal phenotypes more
441 difficult. The second group of targeted genes contained the conserved putative co-
442 transcriptional factor *vgll2b* and the highly conserved membrane bound arrestin *arrdc3a.* Both
443 genes showed specific defects in notochord morphology and structure when targeted and no
444 overt pleiotropic phenotypes. This argues for functional roles for these genes that are likely to
445 be notochord specific. The precise cellular defects caused by these two genes remain unclear
446 although in both cases vacuolated cells appeared morphologically normal. It is clear, though,
447 that targeted notochords appear unable to withstand the high mechanical strain and buckle
448 under pressure. It remains a challenge for the future to decipher the genetic networks of these
449 genes and to assess whether their roles are functionally conserved in higher vertebrates. All
450 in all, using a simple, targeted, reverse-genetics approach, in combination with publicly
451 available data from single cell transcriptomics (Briggs et al. 2018; Farrell et al. 2018), we
452 believe we have implicated new players in correct vertebrate notochord integrity. This
453 methodology can be easily adapted to other contexts and promises to aid in the study of
454 neglected genes with potentially important functions.
455
456
457 **Notochord vacuolated cells during development**
458
459 We made use of the newly generated *Tg(desmogon:EGFP)* line to address the formation and
460 growth dynamics of notochord vacuolated cells during development. It has previously been
461 reported that one vacuole exists per vacuolated cell under homeostatic conditions (Ellis et al.

462 2014) and therefore vacuole growth can be used as a proxy for cellular volume growth. Our
463 results confirm that vacuolated cells grow in volume over time as has been reported before
464 (Ellis et al. 2013; Ellis et al. 2014) and reveal that they do so anisotropically, changing their
465 morphology in the process from more roundish to more oblique shapes. This might be due to
466 the increased cellular packing as the notochord expands. While it has been previously shown
467 that notochords extend over time and that this supports axis elongation in vertebrate embryos
468 (Ellis et al. 2014; Garcia et al. 2017; Ellis et al. 2013), it is still unclear exactly how this growth
469 and expansion is coordinated. A possible mechanism could be that a morphogen gradient
470 synchronizes the growth of neighbouring cells in an orderly fashion. Our dynamic data, in both
471 medaka and zebrafish embryos, argues against the presence of such a signal. We reveal that
472 the growth of vacuolated cells in Medaka and Zebrafish is an incremental one-way process
473 that is locally uncoordinated; neighbouring vacuolated cells grow at different rates. This
474 strongly suggests cell-autonomous mechanisms of vacuolated cell growth, how this is
475 coordinated globally to eventually reach an equivalent size remains unclear and constitutes an
476 interesting avenue for future research. It could be that the final size reached is close to the
477 physiological limit as has been previously suggested (Ellis et al. 2014). On the global growth
478 of the notochordal tissue we report a previously unrecognized bi-directional growth mode
479 where the growth initially driven in the mid-section displaces the posterior and anterior
480 segments of the tube to their respective ends.
481
482 In addition to incrementing their size cell-autonomously we report that the number of
483 vacuolated cells increases as the notochord grows. However, in line with previous
484 observations from Zebrafish (Garcia et al. 2017), we have observed no cell division of
485 vacuolated cells. To characterize the initial steps of vacuolated cell formation during notochord
486 development we employed a highly temporally resolved 4-D approach. We observed that
487 vacuolated cells arise from disc-shaped precursors as previously reported (Melby et al. 1996;
488 Dale & Topczewski 2011). Sparse labelling of these *desmogon*+ precursors in developing
489 Zebrafish notochords combined with long-term live-imaging revealed a hitherto unrecognized

490 *in vivo* behavioural heterogeneity of the disc-shaped precursors. Either they directly
491 differentiate into vacuolated cells (forgoing any division), or they generate sheath cells by
492 undergoing a dorso-ventral symmetric division, that could be followed by further amplifying
493 rounds of mitosis. When considering the position along the AP axis, the developmental time
494 and the levels of EGFP+ expression, we were unable to reliably predict the output of a
495 precursor cell. It seems plausible therefore that the decision to form a vacuolated or sheath
496 cell is not predetermined nor controlled by tissue-level morphogens, but rather depends on
497 sensing the needs of the growing notochord tube in a local manner. Indeed, it has been
498 previously reported that Notch-Jag1 signalling is important in the balance between vacuolated
499 and sheath cell formation (Yamamoto et al. 2010), suggesting that fate acquisition could be
500 resolved locally among neighbouring cells. Complementarily, it is possible that local
501 mechanical forces that arise during the expansion of the tube could operate on inherently
502 plastic disc-shaped precursors and contribute to adopting vacuolated or sheath cell identity.
503
504
505 **Notochord vacuolated cells in regeneration**
506
507 It has been recently shown that Medaka hearts and retinas have a vastly reduced regenerative
508 potential as compared to Zebrafish (Lust & Wittbrodt 2018; Ito et al. 2014; Lai et al. 2017).
509 However, we have previously reported that Medaka neuromasts are able to regenerate
510 efficiently (Seleit, et al. 2017), and the same happens after mechanical amputations on the
511 caudal fin (Katogi et al. 2004) and injuries to the liver (Van Wettere et al. 2013). It therefore
512 seems that Medaka has a highly variable tissue-specific regenerative capacity (Kang et al.
513 2016). We wondered whether Medaka can regenerate lost notochord vacuolated cells. It has
514 been shown in Zebrafish that loss of *caveolae* mutant vacuolated cells in response to
515 mechanical strain triggers an efficient regeneration response (Garcia et al., 2017). This is
516 mediated by sheath cells that invade the inside of the notochord tube and trans-differentiate
517 into vacuolated cells (Garcia et al., 2017). Localized laser-ablation of vacuolated cells in
518 Medaka leads to a very similar process as in Zebrafish where small vacuolated cells
519 specifically invade the injury site. Interestingly, these invading cells start growing in size

520 asynchronously mirroring the un-coordinated nature of growth that we observe for vacuolated
521 cells during development. The appearance of small vacuolated cells during regeneration is
522 another reminiscent feature of what we report during notochord development. Indeed, a
523 proportion of sheath cells formed from dividing precursors during development do initially
524 contain small vacuoles that highly resemble the cells participating in the regenerative
525 response. This suggests two things; a) the presence of sub-populations of sheath cells that
526 display distinct behaviours both during development and regeneration (Lopez-Baez et al.,
527 2018), b) sheath cells participating in the regenerative response most likely re-acquire a small
528 vacuole and could thus be reverting to an earlier state in their developmental history.
529 Reactivation of developmental programs has been a hallmark of efficient regeneration in a
530 variety of models (Tanaka & Galliot 2009; Rodrigo Albors et al. 2015; Kaloulis et al. 2004) and
531 it seems likely that this takes place in the notochord of Medaka after vacuolated cell loss.
532
533 The highly specific spatially localized response to vacuolated cell injury we observe in Medaka
534 indicates that there are mechanisms in place that can sense injured tissue without the need to
535 activate a global regeneration program (LoCascio et al. 2017). Indeed, it has been shown that
536 the release of vacuolated cell contents upon apoptosis can trigger a local regenerative reaction
537 from neighbouring sheath cells (Garcia et al. 2017). A similar process can therefore be
538 occurring in Medaka. Interestingly, when we ablated a small part of the peri-notochordal
539 membrane this led to vacuolated cell leakage at the injury site. As the vacuolated cell leakage
540 continued we witnessed the activation of a global regenerative response anterior and posterior
541 to the original injury site. This could be observed by the presence of small vacuolated cells
542 along the entire length of the notochord. It therefore seems likely that sheath cells can also
543 respond to injury without specific vacuolated cell death, suggesting that sheath cells might be
544 able to sense other stresses like tissue tension. It has recently been reported in Zebrafish that
545 a *wilms*+ subpopulation of sheath cells gets activated in response to a coarse needle injury to
546 the notochord (Lopez-Baez et al. 2018). This sub-population mainly forms scar-tissue that acts
547 as a stopper to maintain notochordal integrity (Lopez-Baez et al. 2018). In Medaka, leakage

548 of vacuolated cells at the site of injury indicates that the peri-notochordal membrane was not
549 efficiently repaired. It is tempting to speculate that this is due to the absence or delayed
550 activation of the wilms+ subpopulation of sheath cells. Overall, our results strongly argue for
551 the presence of distinct injury-sensing mechanisms in sheath cells (dependent and
552 independent of vacuolated cell death). We also report the existence of two regenerative
553 responses in Medaka notochords, one spatially localized and the other global, that depend on
554 the type of injury sustained. Our data positions vacuole re-acquisition by sheath cells as the
555 key step for replenishing vacuolated cells regardless of the type of injury sustained. Identifying
556 the molecular trajectories sheath cells traverse will allow a better understanding of the existing
557 heterogeneities among and plasticity of sheath cells both during development and
558 regeneration. This will in turn allow a more targeted exploitation of the potential of sheath cells
559 in treating notochordal and by extension spinal cord defects in vertebrates.

Figure Legends

Figure 1 d*esmogon* is a desmosomal cadherin that labels the notochord throughout embryogenesis in Medaka.

(A) *in-situ* hybridization on *desmogon* in stage 33 medaka embryos reveals strong enrichment in the notochord. Scalebar=20 microns (B) mosaic injection of desmogon:EGFP in medaka embryos stage 30, labels the notochord. Scale bar=100um (C-D) Transgenic line *Tg(desmog:EGFP)* labels the notochord in Medaka at stage 42 embryos. Scalebar=100 microns (E-F) Maximum projection of mosaic injected (E) and *Tg(desmog:EGFP)* (F) labelling notochord vacuolated cells and a proportion of covering sheath cells. Magenta arrows indicate vacuolated cells and yellow asterisks sheath cells. Scalebar= 50 microns (G) Longitudinal EM section between vacuolated cells connected by desmosomes (black asterisk) Scale bar= 1 micron (G') Desmosomes and caveolae connecting vacuolated cells Scale bar = 0.2 micron. (H) Longitudinal EM section showing desmosomal connections between sheath cells and vacuolated cells scale bar= 1 micron. (I) Cross-section EM showing desmosomal connections between two sheath cells in addition to desmosomes between sheath cells and vacuolated cells scale bar= 1 micron.

Figure 2 Live-imaging of *Tg(desmog:EGFP)* reveals bi-directional growth dynamics of the Medaka notochord. (A) Single plane of 3-4dpf *Tg(desmog:EGFP)* embryo showing vacuolated cells, notice more circular shape and small size compared to (B) 5-6dpf (*Tg)*desmogon:EGFP, bigger and oblique vacuolated cells. n>10. Scalebar=50 microns. (C-C'') SPIM time-lapse imaging *of desmogon*+ vacuolated cell growth over time highlighted with yellow and magenta asterisks (n>10 vacuolated cells in 3 embryos at 4-5dpf and n>10 vacuolated cells in 2 embryos at 3-4dpf). Scalebar=20microns. (D) Schematic diagram of different sectors of the notochord at the anterior and posterior tip, the growth of the tube is driven bi-directionally from the mid-section. (E-E') Vacuolated cells at the anterior end of notochord are displaced more anteriorly as the tube grows from the mid-section. Two outlined

589 vacuolated cells at the anterior end of the growing notochord tube are labelled at t0 (magenta
590 and yellow dotted lines) and traced over time t1 distance between t0 and t1 indicative of
591 displacement more anteriorly. Scalebar=30 microns. Time in hours. (F-F') Disc-shaped
592 precursors at the posterior end of notochord are displaced more posteriorly as the tube grows
593 from the mid-section. Two disc-shaped precursors at the posterior end of the growing
594 notochord tube are labelled at t0 (magenta and yellow dotted lines) and traced over time t1
595 distance between t0 and t1 indicative of displacement more posteriorly. Scalebar=30 microns.
596 Time in hours. N=3 independent embryos.
597
598 **Figure 3 Bi-potent disc-shaped precursor population is fate-restricted at single cell level**
599 (A) Mosaic injected medaka embryo *desmog:EGFP* showing the presence of disc-shaped
600 precursors at the posterior tip of the growing notochord tube. (B) independent clones of sheath
601 cells and vacuolated cells occur in mosaic injected fish. (C-C'') Time-lapse imaging of posterior
602 tip of growing Medaka notochord shows the differentiation dynamics of disc-shaped
603 precursors. Two disc-shaped precursors are labelled (magenta and yellow dot). The magenta
604 labelled precursors start differentiating into a vacuolated cell while the yellow dot labelled
605 precursor undergoes a dorso-ventral division leading to the formation of two sheath cells. Time
606 in hours (D) Disc-shaped precursors at the growing tip of the medaka notochord are fate-
607 restricted and either generate vacuolated cells without dividing or sheath cells after dorso-
608 ventral division. Total disc-shaped precursors followed= 23 in 3 embryos. Scale bars are 20um
609 in A, 1mm in B, and 30 um in C.
610
611 **Figure 4 Local and global regeneration dynamics after notochord injury**
612 (A-A'')*Tg(desmog:EGFP)* 6dpf embryo directly post laser ablation of vacuolated cells. Ablation
613 area indicated by magenta lines. Vacuolated cells in the ablated zone are missing. Vacuolated
614 cells outside ablation zone are intact and morphologically normal. Scalebar= 100 microns. (B-
615 B'') Same embryo 5 days post injury, notice the presence of small vacuolated cells specifically
616 in the site of injury, vacuolated cells grow in size as compared tp 48 hours post injury see

617 supplement, notochord is intact. Scalebar= 100 microns. n=8 embryos. (C-C'') Ablation of
618 vacuolated cells and lower lining of notochord tube. (D-D'') 5 days post injury magenta arrow
619 highlights growing leakage of *desmogon*+ vacuolated cells outside of the notochord. Failure to
620 repair and correctly regenerate lower tube lining is evident. Gross morphological defects
621 apparent over entire length of notochord. Notice the appearance of small vacuolated cells
622 throughout the notochord. Scalebar= 100 microns. n=3 embryos.
623
624 **Figure 5 Gross morphological defects in the notochord of *vgll2b, arrdc3a and***
625 ***desmogon* CRISPR injected embryos**
626 (A) Overall morphology of control *oca2* gRNA & Cas9 injected notochord in
627 *Tg(desmogon:EGFP)*(B-B'') *vgll12b* gRNA1,2 & Cas9 injected into *Tg(desmog:EGFP)* results
628 in morphological defects in the notochord. Notice magenta arrow where notochord is twisted,
629 overall notochord bending observed. Scale bar=100microns. Embryos with phenotypes in
630 notochord 66/120. 79% of embryos survive to stage 42. (C-C'') *arrdc3a* gRNA1,2 & Cas9
631 injected into *Tg(desmog:EGFP)* results in notochord bending. Scalebar=100microns.
632 Embryos with phenotypes 29/97. 77% of embryos survive to stage 42. (D-F)
633 Strong phenotypes in *desmogon* CRISPR injections with gross morphological defects in
634 notochord integrity and notochord buckling and bending. maximum projections.
635 Scalebar=100 microns. Embryos with notochord phenotypes 65/160. Over 90% of embryos
636 survive to stage 42.
637
638 **Figure 6 *desmogon* mutants exhibit notochordal lesions and vacuolated cell collapse.**
639 (A)Control CRISPR injected *Tg(desmog:EGFP)* with o*ca2* gRNA1,2 & Cas9. Single plane.
640 Scalebar=100 microns. (B, C) *desmogon* gRNA1, 2, 3 & Cas9 injected into
641 *Tg*Desmogon:EGFP results in local collapse of vacuolated cells and lesions in the notochord.
642 Single plane. Scalebar=100 microns. (D) Stable *desmogon* CRISPR mutant line recapitulates
643 phenotypes observed in the injected generation Scalebar=100microns. (E) Alizarin red bone
644 staining on *wt* 7days post hatch Medakas shows the highly ordered and regularly sized and

645 spaced vertebral segmentation. (F-G) Alizarin red bone staining on *desmogon* Crispants and
646 stable mutants shows the presence of defects in vertebral size (black arrows in F) and fused
647 vertebrae (black arrows in G). Scale bars on E, F and G= 30 microns.
648
649 **Figure 7 EM on *desmogon* mutants shows normal desmosomes but disrupted**
650 **vacuolated cellular morphology and evidence of a regenerative response**
651 (A-C) EM imaging reveals the presence of desmosomes between vacuolated and sheath cells,
652 and vacuolated cells in *desmogon* mutants. Scale bar= 1 micron in A and B. Scale bar=0.2
653 microns in C. (D) Longitudinal EM section through wild-type stage 42 medaka notochords with
654 highly ordered vacuolated cell arrangement (E) Longitudinal EM section through lesioned
655 *desmogon* mutant stage 42 notochords, notice the structural disorganization, vacuolated cells
656 with varying sizes (yellow arrows), invading sheath cells (black asterisk) and evidence of
657 collapsed vacuolated cells. (F-F') Longitudinal EM section on *desmogon* mutant notochords
658 reveals the presence of collapsed vacuolated cells. (G) Small vacuolated cells are present in
659 Longitudinal sections of EM in *desmogon* mutants and can be clearly distinguished from the
660 neighboring vacuolated cells and sheath cell.
661

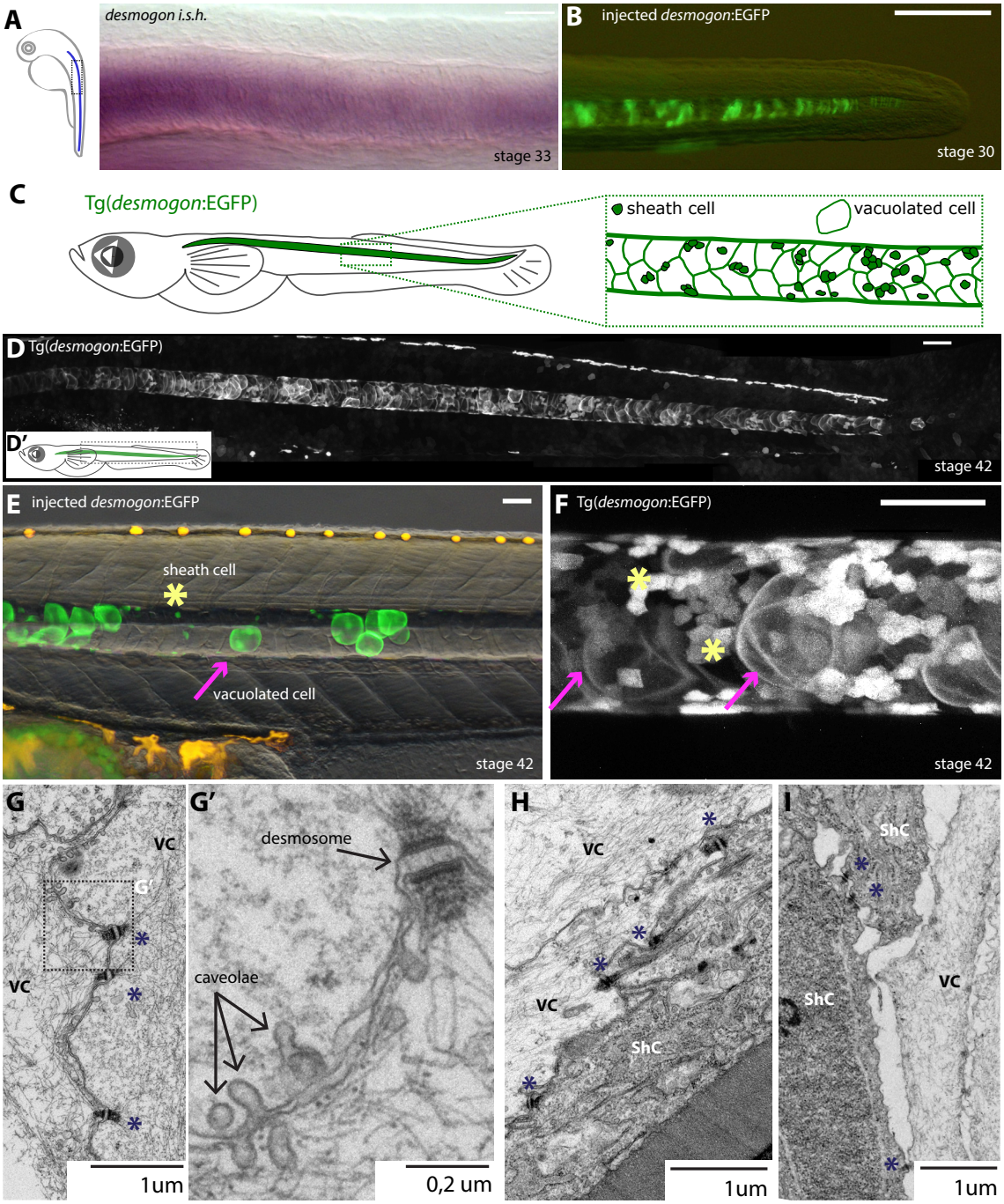

Seleit *et al*, Figure 1

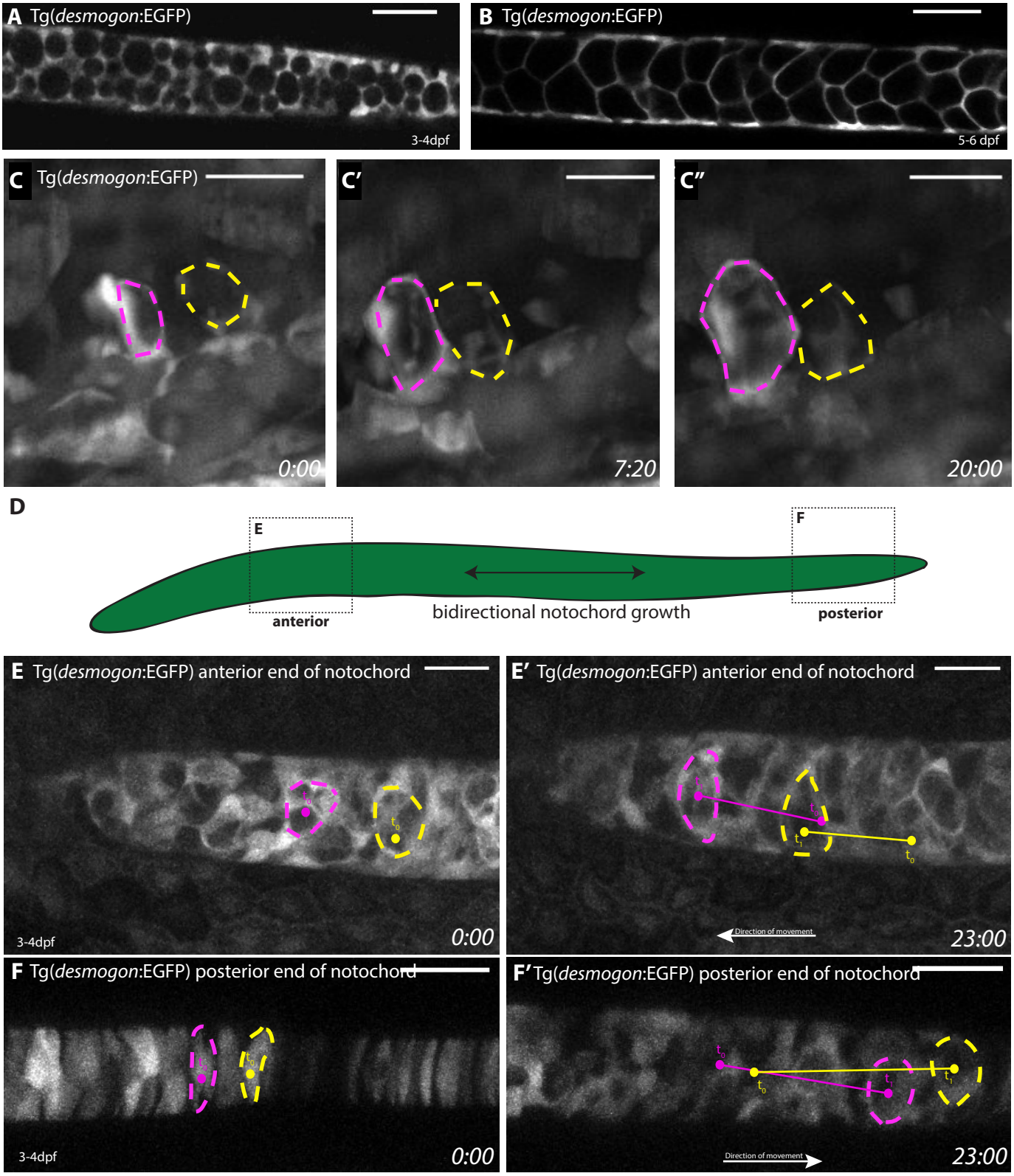

Seleit *et al*, Figure 2

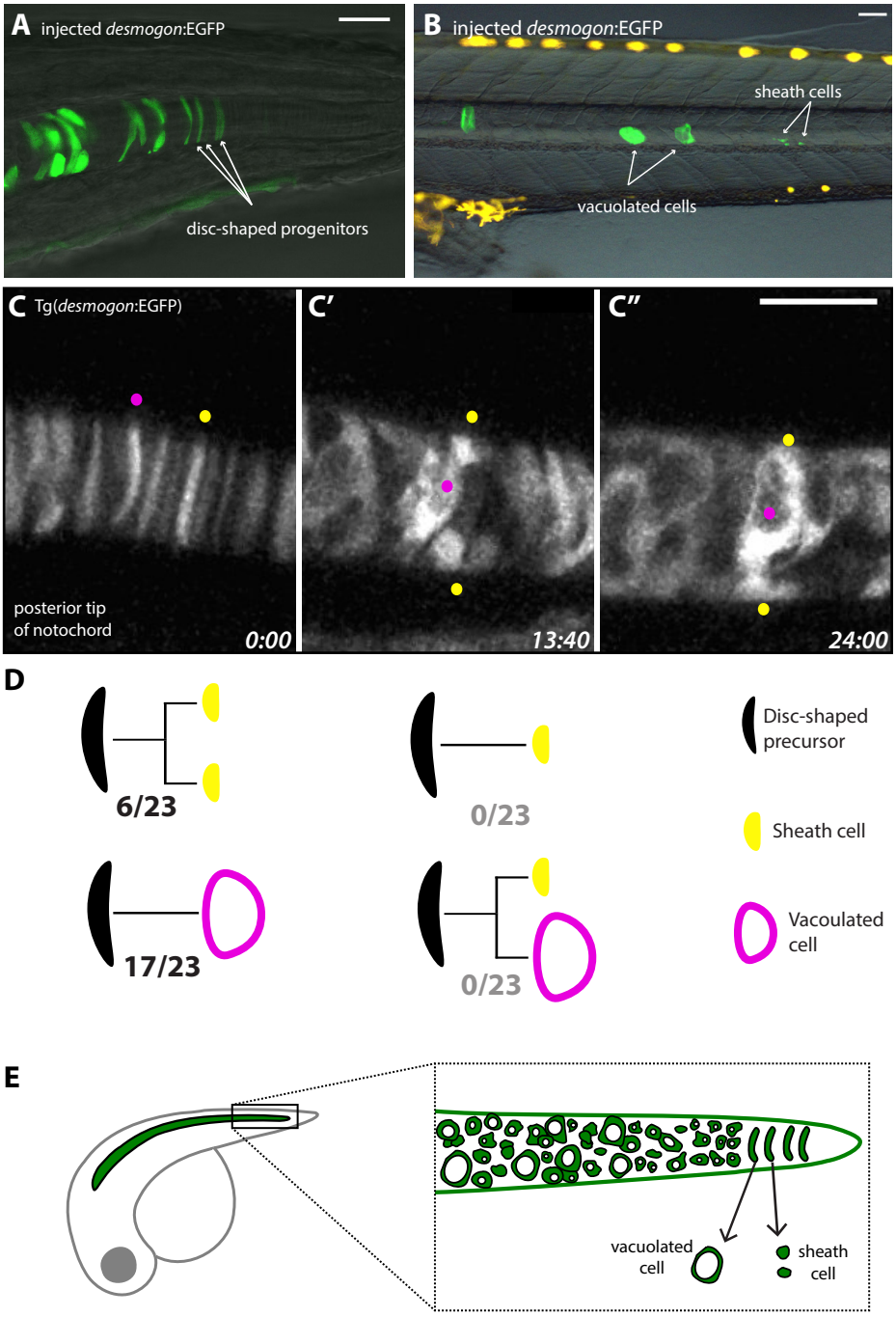

Seleit *et al*, Figure 3

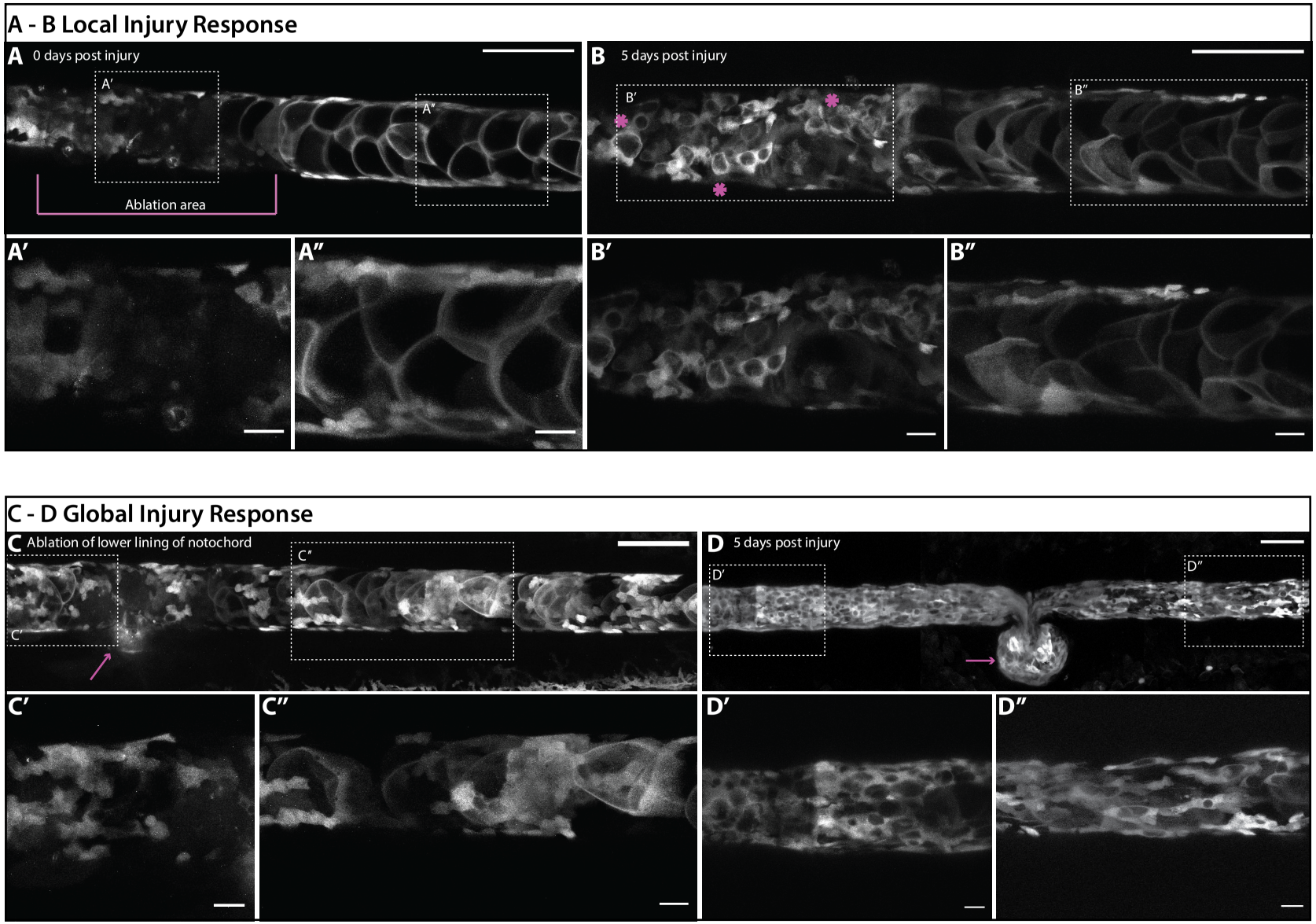

Seleit *et al*, Figure 4

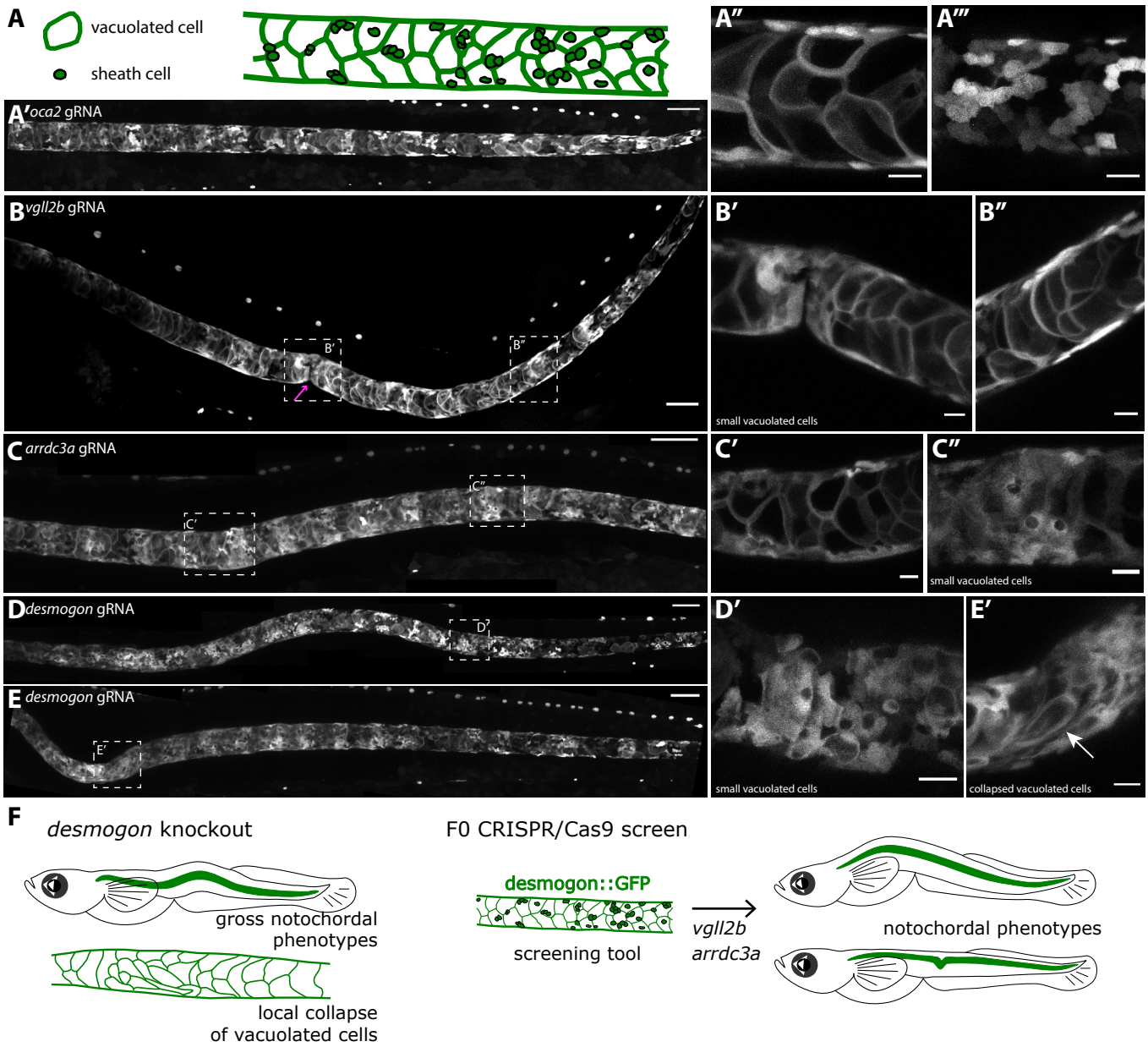

Seleit *et al*, Figure 5

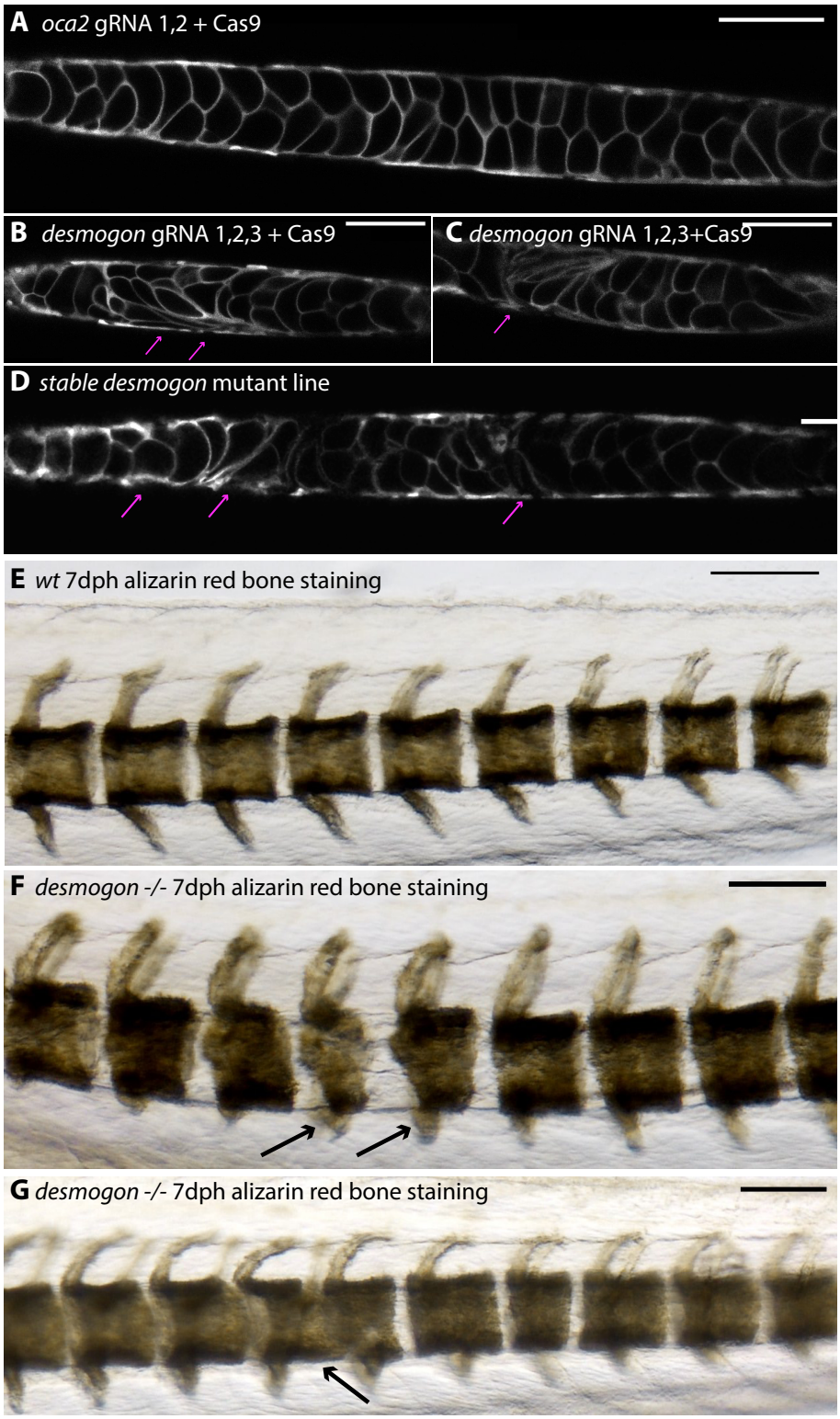

Seleit *et al*, Figure 6

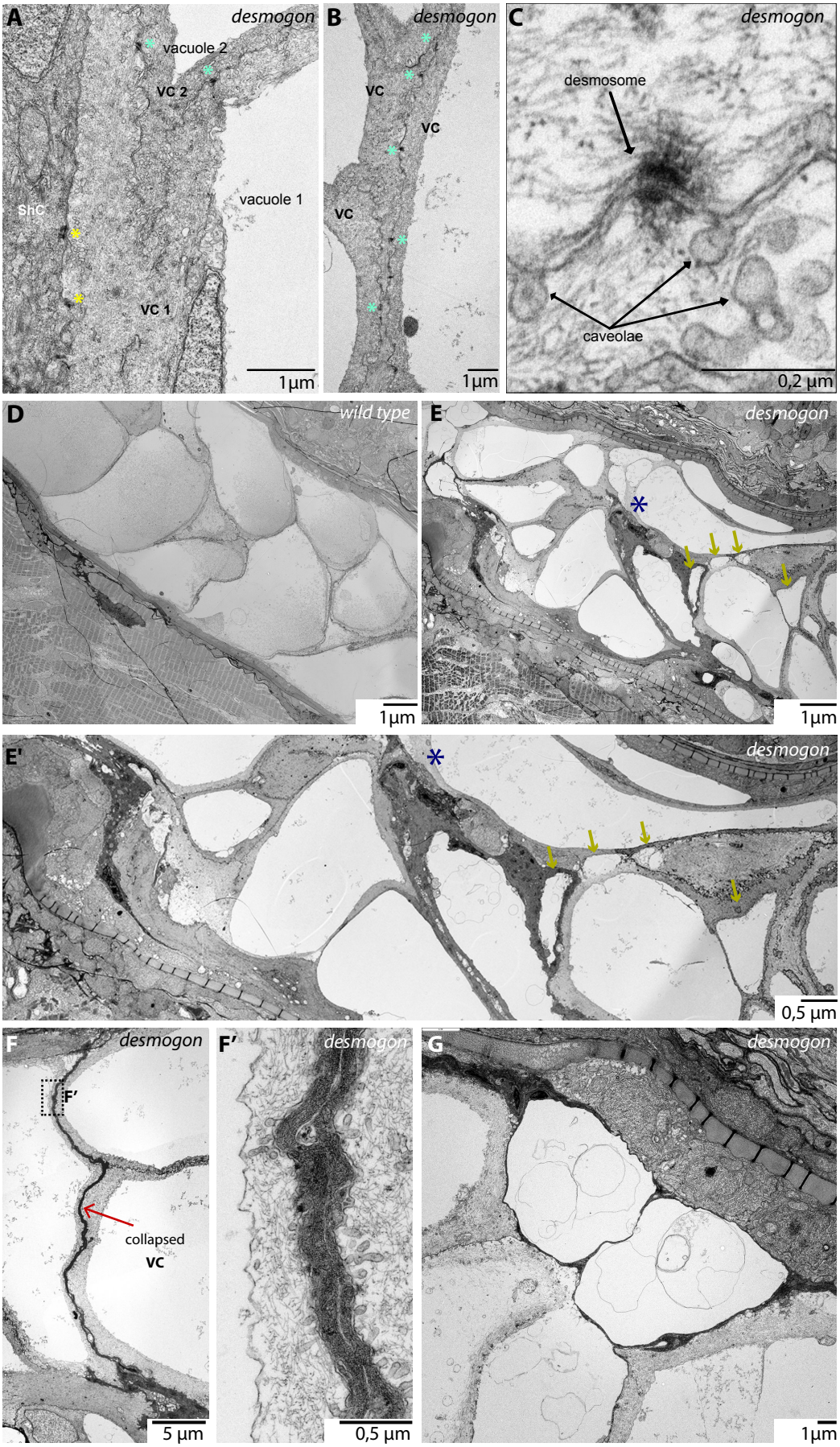

Seleit *et al*, Figure 7

Gene Name	Full name	proposed roles structure and localization	CRISPR Injected F0 Phenotypes %	Phenotypic description
dsgon	*desmogon*	constituent of desmosomal structures, plasma membrane	40,6	local collapses of vacuolated cells, notochord bending, local notochord collapses, no pleotropic effects, highly specific to notochord, 90% of embryos survive to stage 42
vgll2b	*vestigial-like family member 2b*	predicted transcription factor TF/co-factor, nuclear	55	strong phenotypes in the notochord, bending and twisted notochords, spirals of notochord, notochord tube coiling, local collapses of notochord no big pleotropic effects, 79% of embryos survive to stage 42
arrdc3a	*arrestin domain containing 3a*	regulating signal transduction at G protein-coupled receptors	30	wavy notochords, twisted notochords, no strong pleiotropic effects, 77% of embryos survive to stage 42
kcnk6	*potassium two pore domain channel subfamily K member 6*	ion transport, plasma membrane	44,3	kinks and wavy notochords, shorter axis elongation, general growth retardation 73% survive to stage 42
si:dkey-261h17.1	ENSORLG00000015828	cell adhesion, membrane bound	42,1	notochord spirals and twists, wavy notochord, kinks, perturbed axis elongation, 69% of embryos survive to stage 42
pmp22b	*peripheral myelin protein 22b*	helical transmembrane, integral component of membranes,	31,2	strong pleiotropic effects, growth retardation and developmental delays, heart edemas, smaller eyes, wavy notochords, spiral notochords and twists, short axis/failure of axis extension, patterning defects, 58% survive to stage 42

Seleit *et al*, Table 1

Legends of Supplementary Files

Supplementary Movies

Supplementary movie1 *Tg(desmog:EGFP)* labels the Medaka notochord. *Tg(desmog:EGFP)* stage 42 Medaka embryo. Z-stack shows labelled vacuolated cells throughout the notochord and a proportion of sheath cells labelled. Scalebar=100 microns.

Supplementary movie2 3D reconstruction of *Tg(desmog:EGFP*) Medaka notochord. stage 42 Medaka embryo. 3D projection shows the specific labelling of the notochord tube by 2.2kb *desmogon* promoter region. Scalebar=100 microns.

Supplementary movie3 and 4 Asynchronous growth of neighboring vacuolated cells. *Tg(desmog:EGFP)* 4-5dpf embryo. Time-lapse SPIM imaging of growing *desmogon*+ vacuolated cells (3). Time-lapse confocal imaging of growing *desmogon*+ vacuolated cells (4). Notice the anisotropic and autonomous nature of vacuolated cell growth, n>10 vacuolated cells in 3 embryos at 4-5dpf and n>10 vacuolated cells in 2 embryos at 3-4dpf. Scalebar= 20microns. Time in hours.

Supplementary movie5 Bright-field imaging of developing mid-section of medaka notochord shows asynchronous growth of vacuolated cells. 5dpf embryo. Scale bar 30 microns. Time in hours.

Supplementary movie6 Bi-directional growth of the notochord. Anterior section of the developing notochord extends anteriorly. *Tg(desmog:EGFP)* 4-5dpf embryo. Time-lapse imaging of developing anterior section of the notochord reveals a push towards the anterior end. No observable divisions of *desmogon*+ vacuolated cells. n=3 embryos at 4-5dpf and n=2 embryos at 3-4dpf. Scalebar=20 microns. Time in hours.

689

690 **Supplementary movie7** Bi-directional growth of the notochord. Bright-field imaging of anterior
691 section of the notochord reveals push towards the anterior end. Scale bar= 30 microns. Time
692 in hours.

693

694 **Supplementary movie8** Bi-directional growth of the notochord. Bright-field imaging of
695 posterior tip of developing notochord shows that the tube extends posteriorly. Scale bar= 30
696 microns. Time in hours.

697

698 **Supplementary movie9** Bi-directional growth of the notochord. Anterior section of the
699 developing notochord shows individual cells displaced more anteriorly in *Tg(desmog:EGFP)*
700 5dpf embryo . Scale bar= 20 microns. Time in hours.

701

702 **Supplementary movie10** Disc-shaped precursors are located at the posterior tip of the
703 developing Medaka notochord and are pushed posteriorly by the growing tube.
704 *Tg(desmog:EGFP)* 4-5dpf embryo near extending posterior end of the tail. *desmogon*+ disc-
705 shaped precursors can differentiate into vacuolated cells that grow in size over time. Time in
706 hours. Scalebar=30 microns.

707

708 **Supplementary movie11** 3-D reconstruction of disc-shaped precursors. Tg(*desmog:EGFP)*
709 injected *3*dpf embryo near extending posterior end of the tail. Notice the labelling of
710 undifferentiated disc-shaped precursors.

711

712 **Supplementary movie12** Unipotency of disc-shaped precursors in developing medaka
713 notochords. *Tg(desmog:EGFP)* 4-5dpf embryo near extending posterior end of the tail.
714 *desmogon*+ disc-shaped precursors can either differentiate into vacuolated cells that grow in
715 size over time or undergo a dorso-ventral division to produce two sheath cells. Time in hours.
716 Scalebar=30 microns.

717

718 **Supplementary movie13** *desmog:EGFP* labels vacuolated and sheath cells in developing
719 zebrafish notochords. Clones of *desmogon+* cells in 24hpf Zebrafish embryo developing
720 notochord. Both sheath cell clones and vacuolated cell clones are present. Notice the growth
721 of vacuolated cells is locally uncoordinated in Zebrafish as is the case in Medaka. Scalebar=30
722 microns. Time in hours.

723

724 **Supplementary movie14** Unipotency of disc-shaped precursors in zebrafish**.** Clones of
725 *desmogon+* disc shaped precursors in 24hpf Zebrafish embryo developing notochord. Direct
726 differentiation of the anterior disc-shaped precursor into a vacuolated cell. Posterior disc
727 shaped precursor produces two sheath cells after a dorso-ventral division Scalebar=30
728 microns. Time in hours.

729

730 **Supplementary movie15** Dorso-ventral division of disc shaped precursors leads to sheath
731 cell production. Clones of *desmogon+* disc shaped precursors in 24hpf Zebrafish embryo.
732 Notice the presence of small vacuoles in newly formed sheath cells, that disappear over time.
733 Scalebar=30 microns. Time in hours.

734

735 **Supplementary movie16** Presence of small vacuoles in newly formed sheath cells in
736 developing Medaka notochords. Tg(*desmog:EGFP) 4-5*dpf embryo near the mid section of the
737 notochord. Notice the presence of multiple sheath cells with small vacuoles some of which
738 undergo mitotic divisions. Scalebar=20 microns. Time in hours.

739

740 **Supplementary movie17** Pre-injury Z-stack through notochord. *Tg(desmog:EGFP)* 6dpf
741 embryo. Pre-Ablation stack through notochord. Scalebar= 100 microns.

742

743 **Supplementary movie18** Post-injury Z-stack through notochord shows precise ablation of
744 vacuolated cells. *Tg(desmog:EGFP)* 6dpf embryo. Post-laser ablation stack through

745 notochord. Notice the loss of vacuolated cells anteriorly at the site of injury. Scalebar= 100
746 microns.
747
748 **Supplementary movie19** 2 days post-injury Z-stack through notochord reveals presence of
749 small vacuolated cells specifically at the site of injury. *Tg(desmog:EGFP)* embryo. 48hours
750 post-injury stack through notochord. Small vacuolated cells appear specifically in the site of
751 injury. Scalebar= 100 microns.
752
753 **Supplementary movie20** 5 days post-injury Z-stack through notochord reveals the growth of
754 small vacuolated cells specifically at site of injury. *Tg(desmog:EGFP)* embryo. 5 days post-
755 injury stack through notochord. Vacuolated cells grow in size specifically in the site of injury.
756 Scalebar= 100 microns.
757
758 **Supplementary movie21** Injury to peri-notochordal membrane. *Tg(desmog:EGFP)* embryo.
759 Post-ablation stack through notochord. A number of vacuolated cells and the lower lining of
760 the notochord ablated. Scalebar= 100 microns.
761
762 **Supplementary movie22** Lesions of collapsed vacuolated cell in desmogon Crispants.
763 *Tg(desmog:EGFP)* 6-7dpf desmogon gRNA1,2,3 & Cas9 injection. Z-stack through notochord.
764 Strong phenotypes show abnormal notochord lesions. Notice the presence of small vacuolated
765 cells and cellular debris. Overall a disorganized notochord structure is evident. Scalebar= 50
766 microns.
767
768 **Supplementary movie23** Lesions of collapsed vacuolated cells in *desmogon* stable mutants.
769 *Tg(desmog:EGFP)* 6-7dpf desmogon F1 mutant. Z-stack through notochord. Strong
770 phenotypes show abnormal notochord lesions. Phenotype resembles what is observed in the
771 injected generation. Scalebar= 30 microns.
772

773

774 **Supplementary movie24** Control z-stack through *oca2* gRNA injected Tg(desmog:EGFP)
775 embryos. 6-7dpf *oca2* gRNA1,2+ Cas9 injection. Z-stack through notochord. Notice normal
776 notochord and vacuolated cell morphology. Scalebar= 100 microns.

777

778 **Supplementary movie25** *desmogon* gRNA injected embryos exhibit lesions of collapsed
779 vacuolated cells. *Tg(desmog:EGFP)* 6-7dpf Desmogon gRNA1,2,3 & Cas9 injection. Z-stack
780 through notochord. Local collapses of vacuolated cells are evident and vacuolated cell
781 morphology is highly perturbed. Scalebar= 100 microns.

782

783

784 Supplementary Table

785
786 **Table 1** List of genes targeted by CRISPR and quantification of phenotypes in F0 injections.
787 For injection numbers *vgll2b* 66/120 injected fish showed the described phenotype for *arrdc3a*
788 29/97 for *desmogon* 65/160 for *pmp22b* 50/160 for *si:dkey261h17.1* 16/38. Representative
789 phenotypes are shown in supplementary figures.

790

791

792 Supplementary Figures

793

794 **Supplementary Figure 1** (A) Pfam predicted Desmogon protein domains. In green, 3 cadherin
795 domains and in red, a cytoplasmic cadherin domain. Multiple sequence alignment of 12
796 selected species to uncharacterized Medaka protein(H2MRM9). Identity score reveals weak
797 amino acid sequence conservation with closest hits. (B) Comparative genomic alignment of
798 uncharacterized medaka transcript (ENSORLG00000017110) using GENOMICUS shows
799 conservation of the *desmogon* locus in the vast majority of teleost branches; notice the loss of
800 locus in Zebrafish and the Tetraodon. Locus of interest is highlighted by black *desmogon* label.

801 Scheme modified from Genomicus to highlight syntenic genomic region. (C) Choosing of
802 *desmogon* partial 2.2kb promoter, region highlighted in blue. H3K27ac, H3K4me1 and
803 H3K4me2 peaks from UCSC genome browser Medaka blastula stage data at 2.2kb upstream
804 of predicted *desmogon* TSS.
805
806 **Supplementary Figure 2**
807 (A) Classification of vacuoles according to their area shows intermingled distribution of
808 vacuolated cell size during notochordal growth in 3dpf Medaka notochords. (B) Area
809 measurement on 12 paired vacuolated cells at 4 different time-point over a 20-hour period
810 reveals the asynchronous nature of vacuolated cell growth. Neighbouring vacuolated cells
811 share the same colour code and grow at different rates. Area was calculated on maximum
812 projections using standard Fiji software.
813
814 **Supplementary Figure 3**
815 (A, A') Time-lapse recording of clones of vacuolated cells (purple asterisks) and sheath cells
816 (yellow asterisks) labelled after injection of *desmogon*:EGFP plasmid into Zebrafish embryos.
817 Notice the growth of vacuolated cells over time is asynchronous. (B,B') Time-lapse recording
818 of notochord disc-shaped precursor cells labelled in injected zebrafish embryos. One labelled
819 precursor directly trans-differentiates into vacuolated cell (purple asterisks) while the other
820 undergoes a dorso-ventral division giving rise to two sheath cells (yellow asterisks). Scale
821 bar= 30 microns. Time in hours. (C) Quantification of disc-shaped precursor behaviour during
822 development of the notochord in zebrafish N= 4 embryos.
823
824 **Supplementary Figure 4** (A-A'') Local injury response 2 days post injury. Locally restricted
825 appearance of small vacuolated cells in the injured area. (B-B''') Global injury response 2
826 days post injury. Appearance of small vacuolated cells along the entire notochord. (C) Size of
827 perinotochordal injury immediately after laser ablation.
828

829 **Supplementary Figure 5** (A) Schematic view on the *desmogon* locus with exons targeted
830 with gRNAs. (B) Mutant alleles with four base pair addition were isolated by sequencing and
831 TIDE analysis.
832
833 **Supplementary Figure 6** Embryonic phenotypes on F0 CRISPR screen. (A) Brightfield
834 image of a wildtype medaka embryo. (A') Tg(*desmog*:EGFP) wildtype embryo. (B) *desmogon*
835 crispants show vacuolated cell lesions, magenta arrow highlights position of lesion. (C) *vgll2b*
836 crispants show twisted and bent notochords, magenta arrows highlight position of major
837 twists. (D*) arrdc3a* crispants show wavy and bent notochords (magenta arrows). (E) kcnk6
838 crispants show malformed and twisted notochords (magenta arrows). (F) *si:dkey261h17.1*
839 show spirals and twisted notochords (magenta arrows). (G) *pmp22b* crispants show twisted
840 and malformed notochords (magenta arrows).

A

Species	Protein name	Protein entry	Sequence identity %
Oryzias latipes	uncharacterized	H2MRM9	100,0
Fundulus heteroclitus	uncharacterized	A0A147B2M0	66,7
Poeciliopsis prolifica	DSG2	A0A0S7JQR1	65,0
Xiphophorus maculatus	uncharacterized	M4AQR9	59,9
Nothobranchius furzeri	uncharacterized	A0A1A7ZRJ5	59,5
Astyanax mexicanus	uncharacterized	W5KFL2	59,5
Poecilia formosa	uncharacterized	A0A087X6J9	57,3
Danio rerio	dsg2.1	H2EQR6	46,6
Xenopus laevis	dsg2	A0A1L8FYU6	41,6
Homo sapiens	DSG2	Q14126	40,2
Gallus gallus	DSG2	F1NJD5	40,0
Mus musculus	Dsg2	O55111	39,2
Rattus norvegicus	Dsg2	F1LYX9	38,7

B

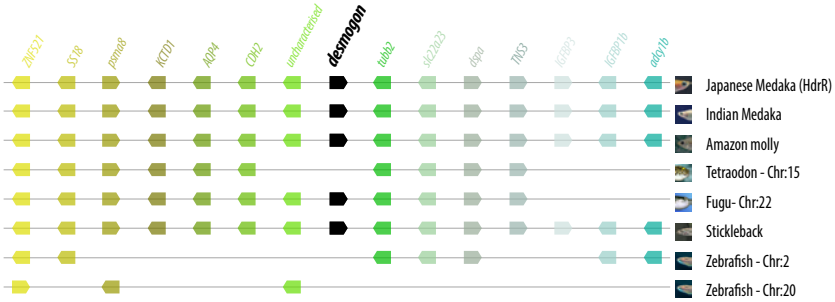

C

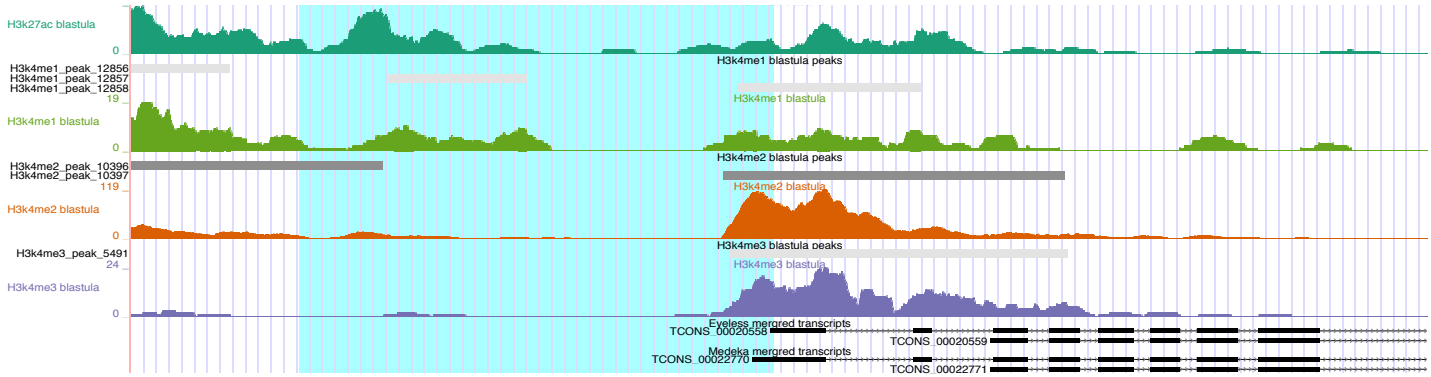

Seleit *et al*, Supplementary Figure 1

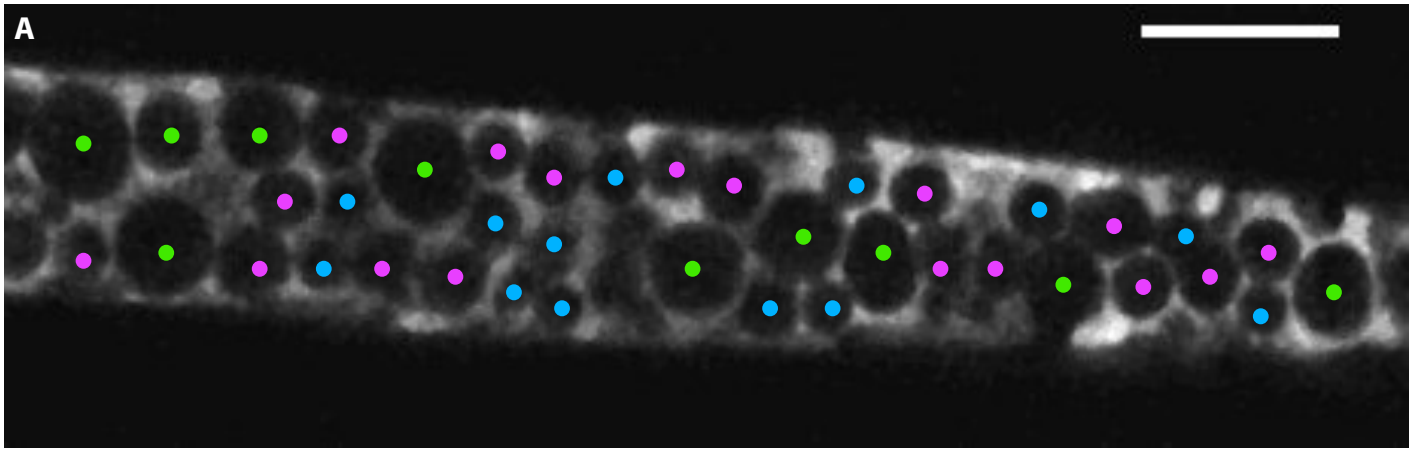

Area in µm² > 300 µm²= ● 200-300 µm²= ● <200µm²= ●

B

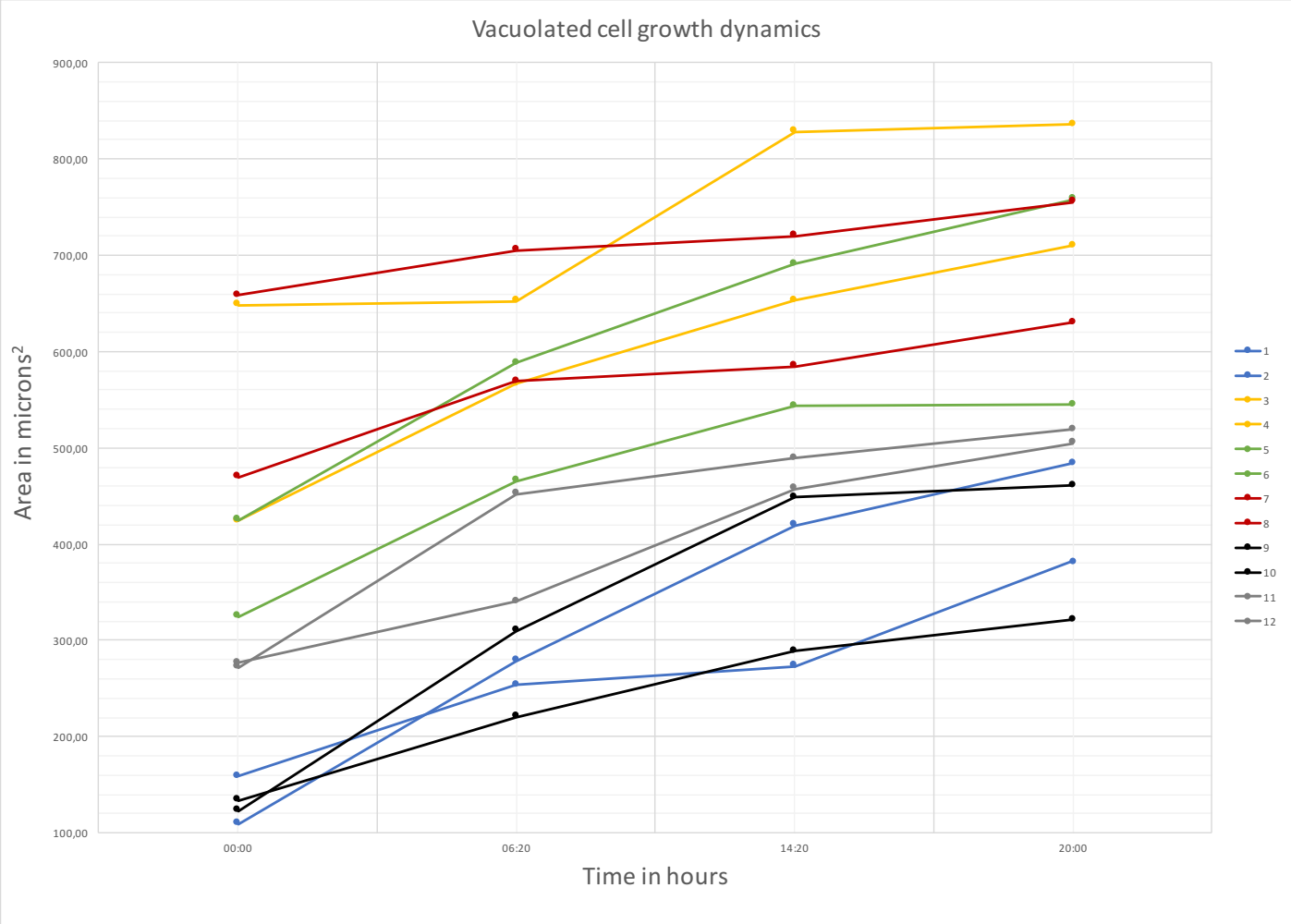

Seleit *et al*, Supplementary Figure 2

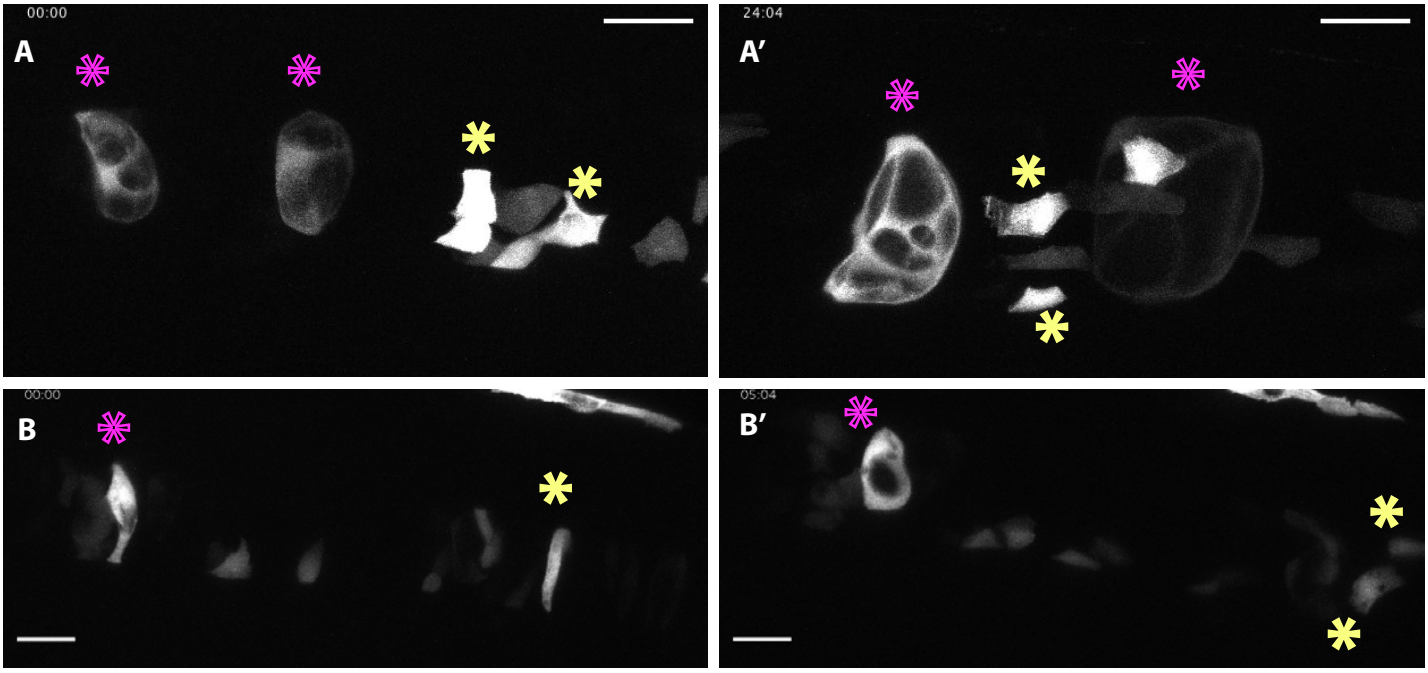

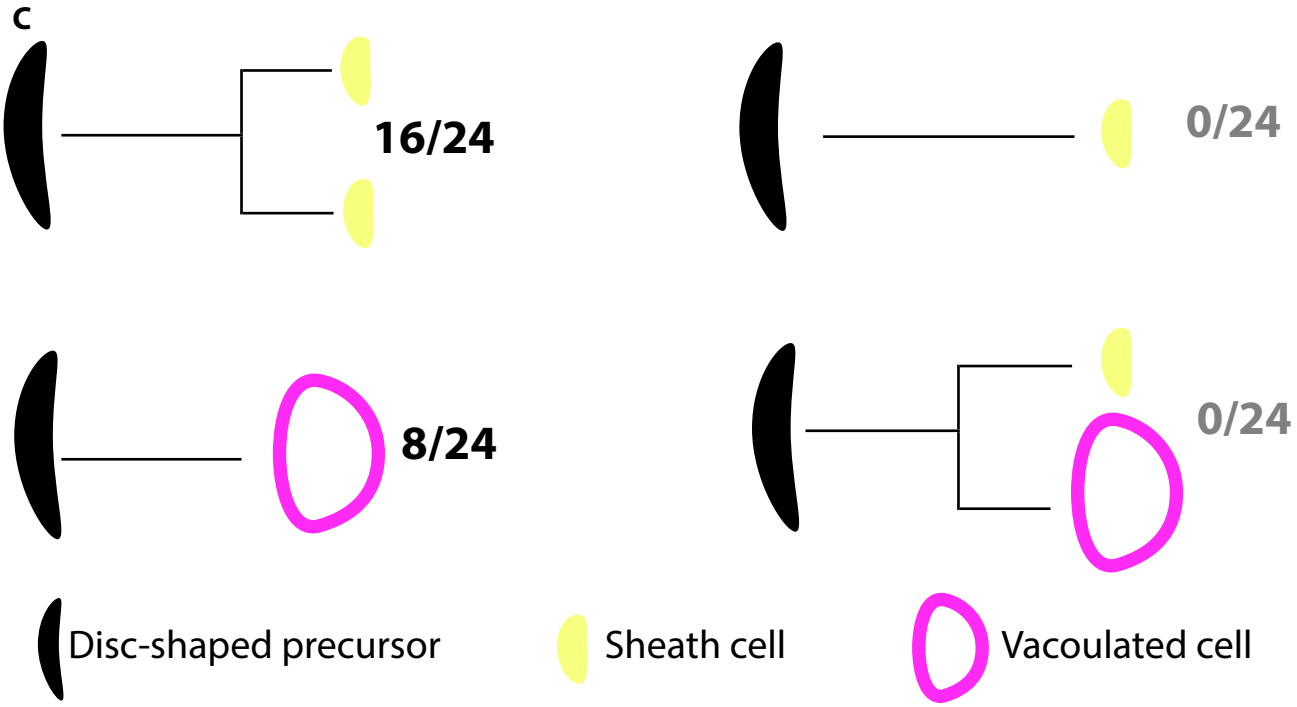

Seleit *et al*, Supplementary Figure 3

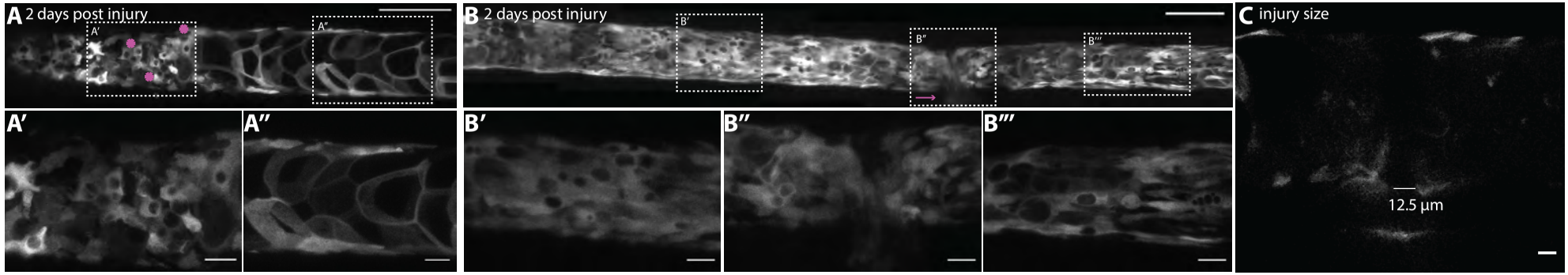

Seleit *et al*, Supplementary Figure 4

A

O.latipes ***desmogon*** locus

1 Kb

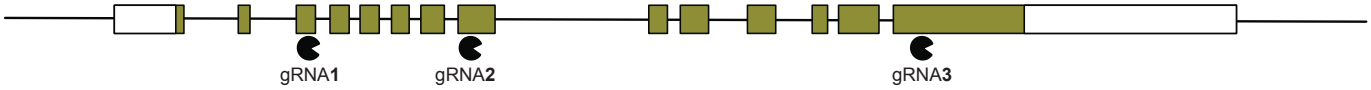

B

gRNA2

desmogon ACTTTGGTGCCAGCTCTTCAGCGGGGTCGTCATCATCATC

desmogon^{+8-4} ACTTTGGTGCCAGCTCTT***GATGCACG***GGGGTCGTCATCATCATC

gRNA2

desmogon ACTTTGGTGCCAGCTCTTCAGCGGGGTCGTCATCATCATC

desmogon^{+4} ACTTTGGTGCCAGCTCTTCAG***GGGT***CGGGGTCGTCATCATCATC

Seleit *et al*, Supplementary Figure 5

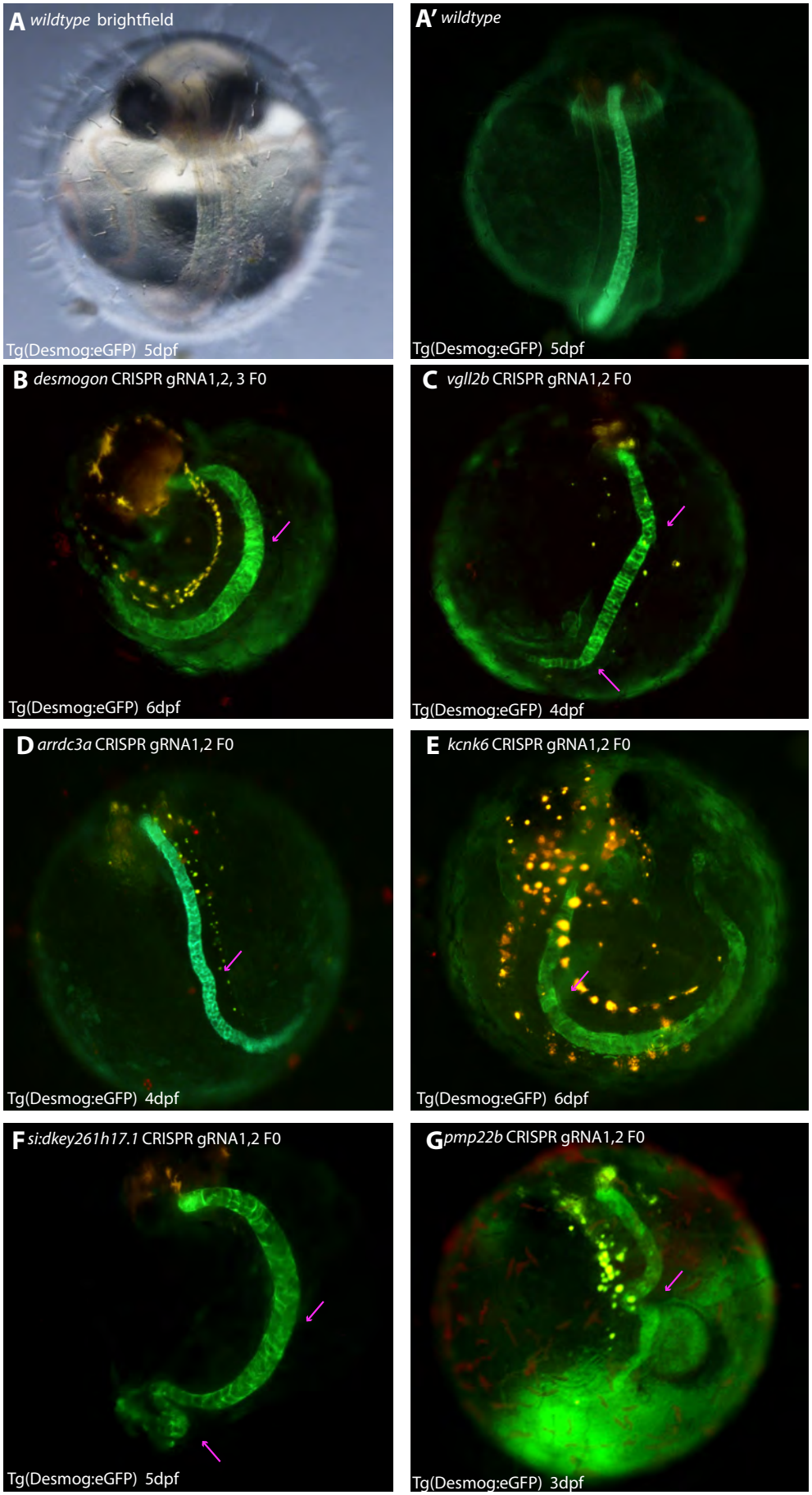

Seleit *et al*, Supplementary Figure 6

Materials and Methods

Fish stocks and generation of transgenic lines

Medaka (*Oryzias latipes*) and Zebrafish (*Danio rerio*) stocks were kept in a fish facility built according to the local animal welfare standards (Tierschutzgesetz §11, Abs. 1, Nr. 1) as described before (Seleit et. al, 2017). Animal experiments were performed in accordance with European Union animal welfare guidelines.(Tierschutzgesetz 111, Abs. 1, Nr. 1, Haltungserlaubnis AZ35–9185.64 and AZ35–9185.64/BH KIT).

The strain used in this study is: Cab (medaka Southern wild type population). Tg(*desmogon*:EGFP) transgenic line was generated for this study by I-SceI mediated insertion, as previously described(Rembold et al. 2006). Briefly, a 2.2kb promoter region upstream of the desmogon CDS (but including the ATG of the first exon) was amplified from Medaka genomic DNA using forward primer (TCGCTGCTTGTTGTGTAGGT) and reverse primer (CATTGGCGCAGTGATTTGAA). The amplified fragment was subsequently cloned by A-tailing into a PGEMTeasy vector (Promega). From there it was sub-cloned into a vector with I-SceI sites and eGFP. This was then injected into Medaka embryos to obtain the transgenic line Tg(*desmogon*:eGFP).

Imaging and Image analysis

Embryos were prepared for live-imaging as previously described (Seleit, et al. 2017a; Seleit, et al. 2017b) 20 mg/ml as a 20x stock solution of tricaine (Sigma-Aldrich, A5040-25G) was utilized to anaesthetise embryos. Glass-bottomed dishes (MatTek Corporation, Ashland, MA 01721, USA) contained the embryos that were in turn covered with low melting agarose (0,6% in ERM). Embryos were screened using an Olympus MVX10 binocular coupled to a Leica DFC500 camera. For image acquisition we used confocal microscopes Leica TCS SPE and Leica TCS SP5 II. Developing notochords were imaged for approximately 1 day using EMBL MuVi-SPIM (Krzic, Gunther, Saunders, Streichan & Hufnagel 2012b) with two illumination objectives (10x Nikon Plan Fluorite Objective, 0.30 NA) and two detection objectives (16X

870 Nikon CFI LWD Plan Fluorite Objective, 0.80 NA). Embryos were placed in glass capillaries
871 using 0,6% low melting agarose at room temperature. Standard Fiji software was used for all
872 image analysis. Stitching was performed using 2D and 3D plugins on Fiji. For mosaic analysis,
873 a *desmogon*:EGFP plasmid was injected embryos into 2 to 4 cell-stage embryos, which were
874 grown until day 9 pf. For the quantification, we selected embryos bearing 1 and up to 4 clusters
875 in the notochord, where clusters were defined as single cells or groups of cell that were at least
876 one somite away from each other.
877

878 **Multi-photon Laser Ablations**

879 A multi-photon laser was used in combination with a Leica TCS SP5 II microscope to perform
880 ablations on vacuolated cells of the notochord and the peri-notochordal membrane in
881 Tg(desmogon:eGFP). 'Point ablations' were chosen along the perimeter of each vacuolated
882 cell. Laser of 880 nm wavelength was used and the power used ranged from 30-35% for 500ms
883 (the time parameter was adjusted in the biological replicates when necessary). The targeted
884 area was immediately imaged post-ablation to checked for signs of cellular bursting, debris
885 and the release of GFP signal.

886 **CRISPR gRNAs and Cas9**

887 Lab-made Cas9 mRNA was transcribed by mMachine Sp6 Transcription Kit (Thermo Fisher).
888 The gRNAs for all targeted genes were designed in-silico using CCtop (Stemmer, Thumberger,
889 et al. 2015). gRNA synthesis was done as previously reported (Stemmer, Thumberger, et al.
890 2015). All genes were targeted with 2 gRNAs against the CDS except *desmogon* where 3
891 gRNAs were designed and injected. The following is a list of gRNA sequences used in this
892 study for each gene.

893 *desmogon gRNA1 (CCCAUAUGGUGUGUUCAGCGUGG) gRNA2*
894 *(UUGGUGCCAGCUCUUCAGCGGGG) gRNA3 (AUCUAUGACUAUGAAGGUCGAGG)*

895 *vgll2b gRNA 1 (UGGGCCCCCAGACAUUCCUUCGG)*

896 *gRNA2(GGGUGCGCCCGUUUCACAGUGGG)*

897 *arrdc3a gRNA1(AAGUUCGUUGGACGGAAUCGAGG)*

898 *gRNA2(AUCCCGCAUGGUGGUCCCAAAGG)*

899 *kcnk6 gRNA1 (GUUCUCCAGCAUCGAGCGGCCGG) gRNA2*

900 *(UGUAUUGUAGUCGCCGGGCGAGG)*

901 *si:dkey- 261h17.1 gRNA1 (GAGCUUGCUGUCACAAGCCUUGG)*

902 *gRNA2(CUGAGUCACUUCAAUCUGCCUGG)*

903 *pmp22b gRNA1(CCUGCUGCACAUUGCUGCACUGG) gRNA2*

904 (CAGCUCUUCACCUUGCAGAAGGG)

905

906 Tg(*desmogon*:eGFP) were injected at the 1 cell stage with a solution containing 15 ng/µl of
907 each gRNA for each gene individually and 150 ng/µl of CAS9 mRNA. The embryos were
908 screened iteratively over the course of development for gross morphological phenotypes and
909 for phenotypes in the notochord. For control injections two gRNAs targeting the *Oca2* locus
910 and Cas9 (Lischik et al. 2018) were injected into Tg(*desmogon*:eGFP) embryos. In order to
911 analyse the mutant alleles, genomic DNA was extracted from *wt* and *desmogon* mutant fish.
912 A PCR flanking the gRNA2 locus was performed using primers *fwd*
913 GCTGGCAGCCTTTGAAATTG *rev* TCGTACCTGACATTGGTGGC. The PCR products were
914 sent to sanger sequencing and also cloned into TopoTA vector (Invitrogen) to distinguish single
915 alleles. The analysis was complemented by using the online software tool TIDE (Brinkman et
916 al., 2014), we were able to isolate the two alleles shown in Supplementary Figure 5.

917

918

919 **Whole-mount *in-situ* hybridization**

920 A 604bp *in situ* probe for *desmogon* was generated from total cDNA of stage 33 medaka
921 embryos by PCR using the following primers *fwd*: TTCTGCGAGATCAGGCTCAC *rev*:
922 AAGGCCCCTCCTCTGTAACT and subsequently A-tailed and cloned into a PGEMTeasy
923 vector (Promega). Sense and anti-sense probes were generated using Sp6 and T7
924 polymerases (Invitrogen) and the *In-situ* hybridization protocol was followed as previously
925 reported in (Stemmer, Schuhmacher, et al. 2015). Hybridisations were performed overnight at
926 65°C then samples were incubated with an antibody against anti-digoxigenin conjugated with
927 AP Fab fragments (1:2000; Roche, 11093274910). Staining was done using NBT/BCIP
928 (Roche).

929 **Electron Microscopy sample preparation and imaging**

930 10 dpf fish from Medaka wt Cab strain and stable Desmogon mutants were placed in a fixative
931 consisting of 2.5% glutaraldehyde and 4% paraformaldehyde in 0.1M PHEM buffer. The
932 fluorescing part of the notochord in mutant fish and equally small pieces of the wt fish was cut
933 out in the fixative and fixation was continued for 30 min at room temperature and at 4˚C
934 overnight. The samples were further fixed in 1% osmium in 0.1M PHEM buffer, washed in
935 water, and incubated in 1% uranylacetate in water overnight at 4˚C. Dehydration was done in
936 10 min steps in an acetone gradient followed by stepwise Spurr resin infiltration at room
937 temperature and polymerization at 60˚C.The blocks were trimmed to get longitudinal sections
938 of the notochord. 70nm thick sections were obtained using a leica UC6 ultramicrotome (Leica
939 Microsystems, Vienna) and the sections were collected on Formvar-coated, copper slot grids
940 and thereafter post-stained with uranyl acetate and Reynold‘s lead citrate. Imaging was done
941 using a JEOL JEM-1400 electron microscope (JEOL, Tokyo) operating at 80 kV and equipped
942 with a 4K TemCam F416 (Tietz Video and Image Processing Systems GmBH, Gautig).

943

944

945 **Transcriptomics data and candidate picking**

946 The targeted genes were selected from single cell transcriptomics data generated by the Klein
947 Lab (Briggs et al., 2018) based on a number of different criteria. First, high enrichment during
948 early development of the notochord in zebrafish. Precisely, candidates were picked from 10,
949 14, 18 and 24 hpf data. Second, the selected genes were checked for conservation across
950 vertebrates. Third the genes had to be well annotated but poorly characterized in both Medaka
951 and Zebrafish. Lastly, a compact and short CDS, simple exon-intron structure/number and
952 limited alternative splicing was favoured to improve chances of efficient mutagenesis with the
953 CRISPR machinery.

954 **Bioinformatics tools**
955
956 ENSEMBL(www.ensembl.org) was used to obtain all the coding sequences and upstream
957 promoter regions for all genes analysed in this study. Supplementary Table 1 and 2 were
958 generated using standard ensembl software using the 1-1 and 1-many orthologue
959 comparisons. Genomic sequence alignments for synteny were performed on ensembl or using
960 GENOMICUS (www.genomicus.biologie.ens.fr/). Protein information and amino acid
961 sequence alignments were done using Uniprot (www.uniprot.org). UCSC
962 (https://genome.ucsc.edu/) genome browser was used for the identification of the promoter
963 region of desmogon. Pfam and PRINTS were used for information on protein domains and
964 conserved motifs (https://pfam.xfam.org/) (http://130.88.97.239/PRINTS/index.php). Single
965 cell transcriptomics data was visualized using
966 (https://kleintools.hms.harvard.edu/paper_websites/wagner_zebrafish_timecourse2018/sprin
967 gViewer.html?coarse_grained_tree) and the selected candidates were obtained from list of
968 enriched genes in developing Zebrafish notochords.

References

Adams, D.S. & Keller, R.E., Koehl, M.A.R 1990. Mechanical Development of the Notochord in Xenopus Early Tail-Bud Embryos. In *Biomechanics of Active Movement and Deformation of Cells*. Berlin, Heidelberg: Springer Berlin Heidelberg, pp. 471–485.

Brinkman E., Chen T., Amendola M. and Steensel B Easy Quantitative Assessment of Genome Editing by Sequence Trace Decomposition. *Nucleic Acids Research* 42, no. 22 (December 16, 2014): e168–68, doi:10.1093/nar/gku936.

Briggs, J.A. et al., 2018. The dynamics of gene expression in vertebrate embryogenesis at single-cell resolution. *Science*, 360(6392), pp.eaar5780–17.

Corallo, D., Trapani, V. & Bonaldo, P., 2018. The notochord: structure and functions. *Cellular and Molecular Life Sciences*, pp.1–20.

Dale, R.M. & Topczewski, J., 2011. Identification of an evolutionarily conserved regulatory element of the zebrafish col2a1a gene. *Developmental Biology*, 357(2), pp.518–531.

Delva, E., Tucker, D.K. & Kowalczyk, A.P., 2009. The desmosome. *Cold Spring Harbor Perspectives in Biology*, 1(2), pp.a002543–a002543.

Ellis, K., Bagwell, J. & Bagnat, M., 2013. Notochord vacuoles are lysosome-related organelles that function in axis and spine morphogenesis. *The Journal of Cell Biology*, 200(5), pp.667–679.

Ellis, K., Hoffman, B.D. & Bagnat, M., 2014. The vacuole within. *BioArchitecture*, 3(3), pp.64–68.

Farrell, J.A. et al., 2018. Single-cell reconstruction of developmental trajectories during zebrafish embryogenesis. *Science*, 360(6392), pp.eaar3131–15.

Fleming, A., 2004. A central role for the notochord in vertebral patterning. *Development*, 131(4), pp.873–880.

Fouquet, B. et al., 1997. Vessel Patterning in the Embryo of the Zebrafish: Guidance by Notochord. *Developmental Biology*, 183(1), pp.37–48.

Garcia, J. et al., 2017. Sheath Cell Invasion and Trans-differentiation Repair Mechanical Damage Caused by Loss of Caveolae in the Zebrafish Notochord. *Current Biology*, 27(13), pp.1982–1989.e3.

Garrod, D. & Chidgey, M., 2008a. Desmosome structure, composition and function. *Biochimica et Biophysica Acta (BBA) - Biomembranes*, 1778(3), pp.572–587.

Garrod, D. & Chidgey, M., 2008b. Desmosome structure, composition and function. *Biochimica et Biophysica Acta (BBA) - Biomembranes*, 1778(3), pp.572–587.

Goonesinghe, A. et al., 2012. Desmosomal cadherins in zebrafish epiboly and gastrulation. *BMC Developmental Biology*, 12(1), p.1.

Gray, R.S. et al., 2014. Loss of col8a1a function during zebrafish embryogenesis results in congenital vertebral malformations. *Developmental Biology*, 386(1), pp.72–85.

1010 Hebrok, M., Kim, S.K. & Melton, D.A., 1998. Notochord repression of endodermal Sonic
1011 hedgehog permits pancreas development. *Genes & Development*, 12(11), pp.1705–
1012 1713.

1013 Ito, K. et al., 2014. Differential reparative phenotypes between zebrafish and medaka after
1014 cardiac injury. *Developmental Dynamics*, 243(9), pp.1106–1115.

1015 Iwamatsu, T 2004. Stages of normal development in the medaka Oryzias latipes.
1016 Mechanisms of development, ISSN: 0925-4773, Vol: 121, Issue: 7-8, Page: 605-18
1017

1018 Jiang, D. & Smith, W.C., 2007. Ascidian notochord morphogenesis. *Developmental*
1019 *Dynamics*, 236(7), pp.1748–1757.

1020 Kaloulis, K. et al., 2004. Reactivation of developmental programs: the cAMP-response
1021 element-binding protein pathway is involved in hydra head regeneration. *Proceedings of*
1022 *the National Academy of Sciences*, 101(8), pp.2363–2368.

1023 Kang, J. et al., 2016. Modulation of tissue repair by regeneration enhancer elements. *Nature*,
1024 532(7598), pp.201–206.

1025 Katogi, R. et al., 2004. Large-scale analysis of the genes involved in fin regeneration and
1026 blastema formation in the medaka, Oryzias latipes. *Mechanisms of Development*, 121(7-
1027 8), pp.861–872.

1028 Koehl, M.A.R., Quillin, K.J. & Pell, C.A., 2000. Mechanical Design of Fiber-Wound Hydraulic
1029 Skeletons: The Stiffening and Straightening of Embryonic Notochords. *American*
1030 *Zoologist*, 40(1), pp.28–041.

1031 Krzic, U., Gunther, S., Saunders, T.E., Streichan, S.J. & Hufnagel, L., 2012a. Multiview light-
1032 sheet microscope for rapid in toto imaging. *Nature methods*, 9(7), pp.730–733.

1033 Krzic, U., Gunther, S., Saunders, T.E., Streichan, S.J. & Hufnagel, L., 2012b. Multiview light-
1034 sheet microscope for rapid in toto imaging. *Nature methods*, 9(7), pp.730–733.

1035 Lai, S.-L. et al., 2017. Reciprocal analyses in zebrafish and medaka reveal that harnessing
1036 the immune response promotes cardiac regeneration. *eLife*, 6, p.1382.

1037 Lim, Y.-W. et al., 2017. Caveolae Protect Notochord Cells against Catastrophic Mechanical
1038 Failure during Development. *Current Biology*, 27(13), pp.1968–1981.e7.

1039 Lischik, C.Q., Adelmann, L. & Wittbrodt, J., 2018. Enhanced in vivo-imaging in fish by
1040 optimized anaesthesia, fluorescent protein selection and removal of pigmentation.

1041 Lleras Forero, L. et al., 2018. Segmentation of the zebrafish axial skeleton relies on
1042 notochord sheath cells and not on the segmentation clock. *eLife*, 7, p.15.

1043 LoCascio, S.A., Lapan, S.W. & Reddien, P.W., 2017. Eye Absence Does Not Regulate
1044 Planarian Stem Cells during Eye Regeneration. *Developmental Cell*, 40(4), pp.381–
1045 391.e3.

1046 Lopez-Baez, J.C. et al., 2018. Wilms Tumor 1b defines a wound-specific sheath cell
1047 subpopulation associated with notochord repair. *eLife*, 7, p.239.

1048 Lust, K. & Wittbrodt, J., 2018. Activating the regenerative potential of Müller glia cells in a
1049 regeneration-deficient retina. *eLife*, 7, p.7028.

1050 Melby, A.E., Warga, R.M. & Kimmel, C.B., 1996. Specification of cell fates at the dorsal
1051 margin of the zebrafish gastrula. *Development*, 122(7), pp.2225–2237.

1052 Nixon, S.J. et al., 2007. Caveolin-1 is required for lateral line neuromast and notochord
1053 development. *Journal of Cell Science*, 120(13), pp.2151–2161.
1054
1055 Pourquie, O. et al., 1993. Control of dorsoventral patterning of somitic derivatives by
1056 notochord and floor plate. *Proceedings of the National Academy of Sciences*, 90(11),
1057 pp.5242–5246.

1058 Rembold, M. et al., 2006. Transgenesis in fish: efficient selection of transgenic fish by co-
1059 injection with a fluorescent reporter construct. *Nature protocols*, 1(3), pp.1133–1139.

1060 Rodrigo Albors, A. et al., 2015. Planar cell polarity-mediated induction of neural stem cell
1061 expansion during axolotl spinal cord regeneration. *eLife*, 4, p.664.

1062 Satoh, N., Tagawa, K. & Takahashi, H., 2012. How was the notochord born? *Evolution &*
1063 *Development*, 14(1), pp.56–75.

1064 Seleit, A., Krämer, I., Ambrosio, E., et al., 2017. Sequential organogenesis sets two parallel
1065 sensory lines in medaka. *Development*, 144(4), pp.687–697.

1066 Seleit, A., Krämer, I., Riebesehl, B.F., et al., 2017. Neural stem cells induce the formation of
1067 their physical niche during organogenesis. *eLife*, 6, p.505.

1068 Stemmer, M., Schuhmacher, L.N., et al., 2015. Cavefish eye loss in response to an early
1069 block in retinal differentiation progression. *Development*, 142(4), pp.743–752.

1070 Stemmer, M., Thumberger, T., et al., 2015. CCTop: An Intuitive, Flexible and Reliable
1071 CRISPR/Cas9 Target Prediction Tool. S. Maas, ed. *PloS one*, 10(4), p.e0124633.

1072 Stemple, D.L., 2005. Structure and function of the notochord: an essential organ for chordate
1073 development. *Development*, 132(11), pp.2503–2512.

1074 Stemple, D.L., 2004. The notochord. *Current Biology*, 14(20), pp.R873–R874.

1075 Stemple, D.L. et al., 1996. Mutations affecting development of the notochord in zebrafish.
1076 *Development*, 123, pp.117–128.

1077 Stoeger, T. et al., 2018. Large-scale investigation of the reasons why potentially important
1078 genes are ignored. T. Freeman, ed. *PLOS Biology*, 16(9), p.e2006643.

1079 Tada, M. & Heisenberg, C.P., 2012. Convergent extension: using collective cell migration
1080 and cell intercalation to shape embryos. *Development*, 139(21), pp.3897–3904.

1081 Talbot, W.S. et al., 1995. A homeobox gene essential for zebrafish notochord development.
1082 *Nature*, 378(6553), pp.150–157.

1083 Tanaka, E. & Galliot, B., 2009. Triggering the regeneration and tissue repair programs. In
1084 Development (Cambridge, England). pp. 349–353.

1085 Trubiroha, A. et al., 2018. A Rapid CRISPR/Cas-based Mutagenesis Assay in Zebrafish for
1086 Identification of Genes Involved in Thyroid Morphogenesis and Function. *Scientific*
1087 *Reports*, pp.1–19.

1088 Van Wettere, A.J. et al., 2013. Immunohistochemical characterization of the hepatic
1089 progenitor cell compartment in medaka (Oryzias latipes) following hepatic injury. *Journal*

1090 *of comparative pathology*, 149(4), pp.434–445.

1091 Wopat, S. et al., 2018. Spine Patterning Is Guided by Segmentation of the Notochord
1092 Sheath. *CellReports*, 22(8), pp.2026–2038.

1093 Wu, R.S. et al., 2018. A Rapid Method for Directed Gene Knockout for Screening in G0
1094 Zebrafish. *Developmental Cell*, 46(1), pp.112–125.e4.

1095 Yamada, T. et al., 1991. Control of cell pattern in the developing nervous system: Polarizing
1096 activity of the floor plate and notochord. *CELL*, 64(3), pp.635–647.

1097 Yamada, T. et al., 1993. Control of cell pattern in the neural tube: Motor neuron induction by
1098 diffusible factors from notochord and floor plate. *CELL*, 73(4), pp.673–686.

1099 Yamamoto, M. et al., 2010. Mib-Jag1-Notch signalling regulates patterning and structural
1100 roles of the notochord by controlling cell-fate decisions. *Development*, 137(15), pp.2527–
1101 2537.

Acknowledgments

We would like to thank Sylvia Urbansky and Steffen Lemke for critical input on the manuscript. J. Wittbrodt for the use of confocal and light sheet microscopes and generous support. We would like to thank C. Funaya, S. Gold and S. Hillmer from the EMCF facility at Heidelberg University for the preparation, imaging and processing of the electron microscopy data. We would like to thank Nihad Softic for injections for spare labeling, Pui Oui Hong for help with the genotyping of *desmogon* mutants, and Carina Vibe for the medaka bone staining protocol. We thank E. Leist, M. Majewski and A. Saraceno for fish husbandry.

Funding

Deutsche Forschungsgemeinschaft (SFB 873)

- Ali Seleit
- Karen Gross
- Lazaro Centanin

The funders had no role in study design, data collection and interpretation, or the decision to submit the work for publication.

Competing interests

No competing interests